The Astrophysical Journal, 976:34 (27pp), 2024 November 20 https://doi.org/10.3847/1538-4357/ad7d93


# Subrelativistic Outflow and Hours-timescale Large-amplitude X-Ray Dips during Super-Eddington Accretion onto a Low-mass Massive Black Hole in the Tidal Disruption Event AT2022lri

Yuhan Yao[1,2], Muryel Guolo[3], Francesco Tombesi[4,5,6], Ruancun Li[7,8], Suvi Gezari[3,9], Javier A. García[10], Lixin Dai[11], Ryan Chornock[2], Wenbin Lu[2,12], S. R. Kulkarni[13], Keith C. Gendreau[10], Dheeraj R. Pasham[14], S. Bradley Cenko[10,15], Erin Kara[14,16], Raffaella Margutti[2,17], Yukta Ajay[3], Thomas Wevers[9], Tom M. Kwan[11], Igor Andreoni[10,15,18], Joshua S. Bloom[2,19], Andrew J. Drake[13], Matthew J. Graham[13], Erica Hammerstein[18], Russ R. Laher[20], Natalie LeBaron[2], Ashish A. Mahabal[13,21], Brendan O'Connor[22], Josiah Purdum[23], Vikram Ravi[13], Huei Sears[24,25], Yashvi Sharma[13], Roger Smith[23], Jesper Sollerman[26], Jean J. Somalwar[13], and Avery Wold[20]

[1] Miller Institute for Basic Research in Science, 468 Donner Lab, Berkeley, CA 94720, USA; yuhanyao@berkeley.edu
[2] Department of Astronomy, University of California, Berkeley, CA 94720, USA
[3] Department of Physics and Astronomy, Johns Hopkins University, 3400 N. Charles Street, Baltimore, MD 21218, USA
[4] Physics Department, Tor Vergata University of Rome, Via della Ricerca Scientifica 1, 00133 Rome, Italy
[5] INAF—Astronomical Observatory of Rome, Via Frascati 33, 00040 Monte Porzio Catone, Italy
[6] INFN—Rome Tor Vergata, Via della Ricerca Scientifica 1, 00133 Rome, Italy
[7] Kavli Institute for Astronomy & Astrophysics and Department of Astronomy, Peking University, Beijing 100871, People's Republic of China
[8] Department of Astronomy, School of Physics, Peking University, Beijing 100871, People's Republic of China
[9] Space Telescope Science Institute, 3700 San Martin Drive, Baltimore, MD 21218, USA
[10] Astrophysics Science Division, NASA Goddard Space Flight Center, Greenbelt, MD 20771, USA
[11] Department of Physics, University of Hong Kong, Pokfulam Road, Hong Kong
[12] Theoretical Astrophysics Center, University of California, Berkeley, CA 94720, USA
[13] Cahill Center for Astrophysics, California Institute of Technology, MC 249-17, 1200 E California Boulevard, Pasadena, CA 91125, USA
[14] Kavli Institute for Astrophysics and Space Research, Massachusetts Institute of Technology, Cambridge, MA 02139, USA
[15] Joint Space-Science Institute, University of Maryland, College Park, MD 20742, USA
[16] Department of Physics, Massachusetts Institute of Technology, Cambridge, MA 02139, USA
[17] Department of Physics, University of California, 366 Physics North MC 7300, Berkeley, CA 94720, USA
[18] Department of Astronomy, University of Maryland, College Park, MD 20742, USA
[19] Lawrence Berkeley National Laboratory, 1 Cyclotron Road, MS 50B-4206, Berkeley, CA 94720, USA
[20] IPAC, California Institute of Technology, 1200 E. California Boulevard, Pasadena, CA 91125, USA
[21] Center for Data Driven Discovery, California Institute of Technology, Pasadena, CA 91125, USA
[22] McWilliams Center for Cosmology and Astrophysics, Department of Physics, Carnegie Mellon University, Pittsburgh, PA 15213, USA
[23] Caltech Optical Observatories, California Institute of Technology, Pasadena, CA 91125, USA
[24] Center for Interdisciplinary Exploration and Research in Astrophysics (CIERA), Northwestern University, Evanston, IL 60202, USA
[25] Department of Physics and Astronomy, Northwestern University, Evanston, IL 60208, USA
[26] The Oskar Klein Centre, Department of Astronomy, Stockholm University, AlbaNova, SE-10691, Stockholm, Sweden
*Received 2024 May 16; revised 2024 September 15; accepted 2024 September 16; published 2024 November 12*

## Abstract

We present the tidal disruption event (TDE) AT2022lri, hosted in a nearby (≈144 Mpc) quiescent galaxy with a low-mass massive black hole ($10^4\,M_\odot < M_{\rm BH} < 10^6\,M_\odot$). AT2022lri belongs to the TDE-H+He subtype. More than 1 Ms of X-ray data were collected with NICER, Swift, and XMM-Newton from 187 to 672 days after peak. The X-ray luminosity gradually declined from $1.5 \times 10^{44}$ erg s$^{-1}$ to $1.5 \times 10^{43}$ erg s$^{-1}$ and remains much above the UV and optical luminosity, consistent with a super-Eddington accretion flow viewed face-on. Sporadic strong X-ray dips atop a long-term decline are observed, with a variability timescale of ≈0.5 hr–1 days and amplitude of ≈2–8. When fitted with simple continuum models, the X-ray spectrum is dominated by a thermal disk component with inner temperature going from ∼146 to ∼86 eV. However, there are residual features that peak around 1 keV, which, in some cases, cannot be reproduced by a single broad emission line. We analyzed a subset of time-resolved spectra with two physically motivated models describing a scenario either where ionized absorbers contribute extra absorption and emission lines or where disk reflection plays an important role. Both models provide good and statistically comparable fits, show that the X-ray dips are correlated with drops in the inner disk temperature, and require the existence of subrelativistic (0.1–0.3$c$) ionized outflows. We propose that the disk temperature fluctuation stems from episodic drops of the mass accretion rate triggered by magnetic instabilities or/and wobbling of the inner accretion disk along the black hole's spin axis.

*Unified Astronomy Thesaurus concepts:* Tidal disruption (1696); X-ray transient sources (1852); Supermassive black holes (1663); Time domain astronomy (2109); High energy astrophysics (739); Accretion (14)

*Materials only available in the online version of record: machine-readable table*

## 1. Introduction

### 1.1. Super-Eddington Accretion onto Low-mass Massive Black Holes in Tidal Disruption Events

The detection of $\sim 10^9\,M_\odot$ accreting black holes (BHs) at merely <1 Gyr after the Big Bang (X. Fan et al. 2023) implies that a sustained period of super-Eddington accretion must have occurred in the early Universe. However, the process of BH super-Eddington accretion is observationally poorly characterized due to the fact that the majority of active galactic nuclei (AGN) are accreting at sub-Eddington rates.

Stars that are tidally disrupted outside the event horizon of a massive black hole (MBH) give rise to a panchromatic transient as the disrupted material falls onto the MBH (see S. Gezari 2021 for a recent review). Basic theory for such tidal disruption events (TDEs) predicts that, after the disruption of a star (with mass $M_*$ and radius $R_*$), the mass fallback rate $\dot{M}_{\rm fb}$ initially rises for a fallback timescale of

$$t_{\rm fb} = 41\ {\rm days}\ (M_{\rm BH}/10^6 M_\odot)^{1/2} m_*^{-1} r_*^{3/2} \quad (1)$$

to a peak mass fallback rate of

$$\frac{\dot{M}_{\rm fb,\ peak}}{\dot{M}_{\rm Edd}} = 136 \eta_{-1} m_*^2 r_*^{-3/2} (M_{\rm BH}/10^6\,M_\odot)^{-3/2}, \quad (2)$$

$$\dot{M}_{\rm Edd} = \frac{L_{\rm Edd}}{\eta c^2},\quad L_{\rm Edd} = 1.26 \times 10^{38} (M_{\rm BH}/M_\odot)\ {\rm erg\ s^{-1}} \quad (3)$$

where $m_* = M_*/M_\odot$, $r_* = R_*/R_\odot$, $\eta$ is the accretion radiative efficiency, and $\eta_{-1} \equiv \eta/0.1$. The returned stellar debris quickly circularize to form a compact accretion flow on the timescale of $t_{\rm circ} \lesssim t_{\rm fb}$ (C. Bonnerot et al. 2016; K. Hayasaki et al. 2016; C. Bonnerot & W. Lu 2020; Z. L. Andalman et al. 2022; E. Steinberg & N. C. Stone 2024). For lower-mass MBHs ($M_{\rm BH} \lesssim 10^6\,M_\odot$), $\dot{M}_{\rm fb}$ remains super-Eddington for a few years —radiation is trapped in the disk and puffs up the disk, such that the disk thickness over radius is on the order of unity (M. A. Abramowicz et al. 1988; J. L. Dai et al. 2021). In this case, the viscous timescale is short, and the mass accretion rate is expected to closely follow the $\dot{M}_{\rm fb} \propto t^{-5/3}$ evolution that samples a wide range in a known way (M. J. Rees 1988; C. R. Evans & C. S. Kochanek 1989; E. S. Phinney 1989; G. Lodato et al. 2009; F. De Colle et al. 2012). It is for this reason that TDEs (especially those occurring in lower-mass BHs) provide clean laboratories to understand BH super-Eddington accretion.

While the early time TDE emission might be powered by either reprocessed disk emission at larger radii (A. Loeb & A. Ulmer 1997; B. D. Metzger & N. C. Stone 2016; N. Roth et al. 2016; L. Dai et al. 2018; B. D. Metzger 2022) or adiabatic photon trapping in expanding outflows (Y.-F. Jiang et al. 2016; W. Lu & C. Bonnerot 2020), it is generally expected that direct disk emission should become the dominant component after a few $\times\, t_{\rm fb}$. A rough estimate for the inner disk temperature is the temperature associated with an Eddington luminosity from an order of unity factor times the gravitational radius (A. Ulmer 1999):

$$T_{\rm in} \approx \left[\frac{L_{\rm Edd}}{4\pi (6R_g)^2 \sigma_{\rm SB}}\right]^{1/4} = 59\ {\rm eV}\ (M_{\rm BH}/10^6 M_\odot)^{-1/4}. \quad (4)$$

In lower-mass MBHs, the disk emission should peak in the soft X-ray band. Observationally, however, the soft X-ray emission of many optically selected TDEs in lower-mass MBHs remain much fainter than the UV and optical emission out to $t \gtrsim 1$ yr,[27] indicating that the TDE structure is more complex than predicted by basic theory. Possible explanations for the lack of X-ray emission include a viewing-angle dependence of the optical-to-X-ray ratio for a thick disk (L. Dai et al. 2018; B. D. Metzger 2022), insufficient debris circularization at early times (H. Shiokawa et al. 2015), and significantly reduced mass inflow rate at the inner disk region due to mass loss in line-driven disk winds (M. C. Miller 2015).

### 1.2. AT2022lri

AT2022lri ($\alpha = 02^{\rm h}20^{\rm m}8\overset{\rm s}{.}01$, $\delta = -22^\circ 42' 15\overset{''}{.}21$) was first reported to the Transient Name Server (TNS) by the ATLAS team (as ATLAS22pnz) in 2022 June with an *o*-band detection at 17.2 mag (J. Tonry et al. 2022). It was subsequently detected by the Zwicky Transient Facility (ZTF; E. C. Bellm et al. 2019; M. J. Graham et al. 2019; R. Dekany et al. 2020) survey (as ZTF22abajudi) on 2022 August 14 (MJD 59805.508) with an *r*-band detection at $18.77 \pm 0.04$ mag. On 2022 September 3, this object passed the ZTF Bright Transient Survey (C. Fremling et al. 2020; D. A. Perley et al. 2020) experiment. On 2022 September 17, it passed our TDE selection filter[28] (S. van Velzen et al. 2019), and optical spectroscopy with the Double Spectrograph (DBSP; J. B. Oke & J. E. Gunn 1982) was triggered on 2022 October 11. An initial Neil Gehrels Swift Observatory (hereafter Swift) snapshot was triggered on 2022 October 13, which revealed a bright UV source as well as bright and soft X-ray emission detected by the X-Ray Telescope (XRT; D. N. Burrows et al. 2005). On 2022 October 24, we classified AT2022lri as a TDE (Y. Yao et al. 2022b) based on characteristic broad emission lines shown in its DBSP spectrum (Y. Yao 2022), the blue color ($uvw2 - r \approx -1$ mag), and the luminous soft X-ray detection.

From 2022 October 23 to 2024 March 5, we conducted high-cadence X-ray observations using the Neutron Star Interior Composition Explorer (NICER; K. C. Gendreau et al. 2016; for a total of 845 ks), the XRT (87 ks), and three XMM-Newton exposures (152 ks). Hosted by a low-mass MBH, the X-ray light of AT2022lri remains much in excess of the UV and optical emission. The X-ray luminosity alone is $\gtrsim L_{\rm Edd}$, in line with the basic TDE theory (Section 1.1). What distinguishes AT2022lri from all previously known TDEs is the following:

1. The observed peak 0.3–2 keV flux reached $4.7 \times 10^{-11}$ erg s$^{-1}$ cm$^{-2}$ (1.6 mCrab), making it brighter than all other nonjetted TDEs in the literature. The bright X-ray flux facilitated high-quality X-ray spectroscopy, showing evidence of subrelativistic outflows.
2. The intensive X-ray monitoring campaign, particularly with NICER, uncovered fast large-amplitude (multiplicative factors of ~2–8) X-ray variability on hour–day timescales. The X-ray spectral evolution within such

[27] For example, see AT2018lna, AT2018zr, AT2020vwl, AT2020wey (M. Guolo et al. 2024), AT2020neh (C. R. Angus et al. 2022), and AT2020vdq (J. J. Somalwar et al. 2023).

[28] Before 2023 September, the ZTF team selected nuclear transients by filtering public alerts with the AMPEL broker (J. Nordin et al. 2019).

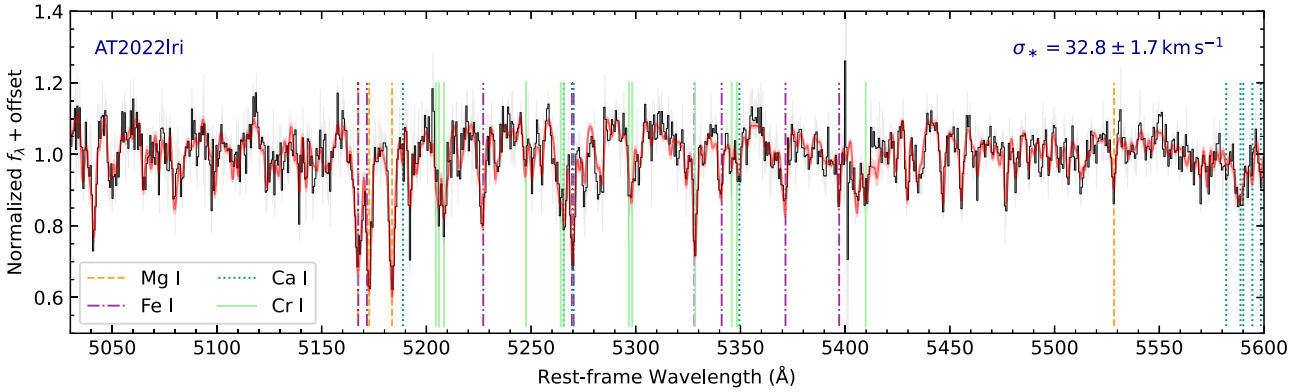


**Figure 1.** ESI spectrum of AT2022lri's host galaxy (black) and the best-fit model (red). Prominent host galaxy absorption lines are indicated by the vertical lines. The median SNR of the fitted wavelength range of 5030–5600 Å is 15.7.

short timescales exhibits rapid inner disk temperature variations.

These distinct X-ray characteristics of AT2022lri provide novel insights into the inner accretion flow of TDEs under super-Eddington accretion.

This paper is structured as follows. Section 2 presents the observation and analysis of AT2022lri's host galaxy. In Section 3, we outline the UV and optical observations, data reduction, and analysis of AT2022lri. In Section 4, we provide a detailed description of the X-ray observations, data processing, and spectral modeling. In Section 5, we discuss our results in context of BH super-Eddington accretion, and compare AT2022lri with other nuclear transients with similar properties. Finally, we summarize our results in Section 6.

UT time is used throughout the paper. We adopt a standard ΛCDM cosmology with matter density $\Omega_{\rm M} = 0.3$, dark energy density $\Omega_\Lambda = 0.7$, and the Hubble constant $H_0 = 70\,\mathrm{km\,s^{-1}\,Mpc^{-1}}$, implying a luminosity distance to AT2022lri of $D_L = 143.8$ Mpc at the redshift of $z = 0.03275 \pm 0.00001$ (see Section 2.1). UV and optical magnitudes are reported in the AB system. We use the extinction law from J. A. Cardelli et al. (1989), assume $R_V = 3.1$, and adopt a Galactic extinction of $E_{B-V,\rm MW} = 0.0158$ mag (E. F. Schlafly & D. P. Finkbeiner 2011). Uncertainties are reported at the 68% confidence intervals, and upper limits are reported at $3\sigma$. Coordinates are given in J2000.

## 2. Host Galaxy Observations and Analysis

### 2.1. Velocity Dispersion

A medium-resolution spectrum was obtained on 2023 August 26.6 using the Echellette Spectrograph and Imager (ESI; A. I. Sheinis et al. 2002) on the Keck II telescope. At this phase, the TDE flux is negligible in the optical band compared with the host galaxy flux (see Section 3). The observation was performed in the Echellette mode with a 0.″75 slit, which gives a resolving power of $R = 5350$ (i.e., $\sigma_{\rm inst} = 24\,\mathrm{km\,s^{-1}}$). The data were processed using the `makee` pipeline following standard procedures. From the median light profile of the traces, we estimated that the half-light radius ($r_{1/2}$) of the galaxy is ≈0.″98. We then extracted the ESI spectrum using a radius of $r_{1/2}$ (i.e., 6.2 pixels), and normalized the spectrum by fitting a spline function to the continuum, with prominent emission and absorption lines masked.

To infer the stellar velocity dispersion ($\sigma_*$), we modeled the ESI spectrum with penalized pixel-fitting (`pPXF`; M. Cappellari & E. Emsellem 2004; M. Cappellari 2017) and the ELODIE v3.1 high-resolution ($R = 42{,}000$) library (P. Prugniel & C. Soubiran 2001; P. Prugniel et al. 2007), following the same steps adopted by Y. Yao et al. (2023). Fitting over the wavelength range of 5030–5600 Å, we derived a redshift of $z = 0.03275 \pm 0.00001$ and a velocity dispersion of $\sigma_* = 32.8 \pm 1.7\,\mathrm{km\,s^{-1}}$. The fitting result is shown in Figure 1. If using a wider wavelength range of 4600–5600 Å, the velocity dispersion remains consistent at $\sigma_* = 32.0 \pm 1.6\,\mathrm{km\,s^{-1}}$.

### 2.2. Morphology and Spectral Energy Distribution Fitting

We employed the multiband imaging decomposition tool GALFITS (R. Li & L. C. Ho 2024, in preparation) to analyze the pre-TDE images of AT2022lri. The data set comprises UV images from the Galaxy Evolution Explorer (GALEX; D. C. Martin et al. 2005), *griy* images from Pan-STARRS1 (K. C. Chambers et al. 2016),[29] *grz* images from the DESI Legacy Imaging Survey (LS; A. Dey et al. 2019), as well as infrared images from the Two-Micron All Sky Survey (M. F. Skrutskie et al. 2006) and the Wide-field Infrared Survey Explorer (E. L. Wright et al. 2010), totaling 16 images. GALFITS performs morphological decomposition and spectral energy distribution (SED) fitting simultaneously by assigning different components distinct structural parameters as well as stellar populations. For GALEX images, we collected the entire image tile encompassing AT2022lri. For other images, a cutout of 4000″ was utilized. This approach ensures adequate sampling of sky pixels, facilitating accurate sky subtraction. For each image, we generated a point-spread function (PSF) by fitting stars within the same field. These stars were selected by crossmatching with the Gaia DR3 catalog (Gaia Collaboration et al. 2023). Subsequently, a 30″ box cutout was applied to all 16 images to serve as the input data for GALFITS. Additionally, we generated a common mask image for all bands to minimize the impact of contaminating sources on GALFITS. The upper left panel of Figure 2 shows the LS *z*-band image, where the mask image is depicted as the shaded region.

During the GALFITS fitting, we tested models featuring both single and double Sérsic components. To define each component, besides two parameters for the position, there are four morphological parameters and five SED-related

[29] The Pan-STARRS1 *z*-band image was excluded due to artifacts resulting from overexposure.

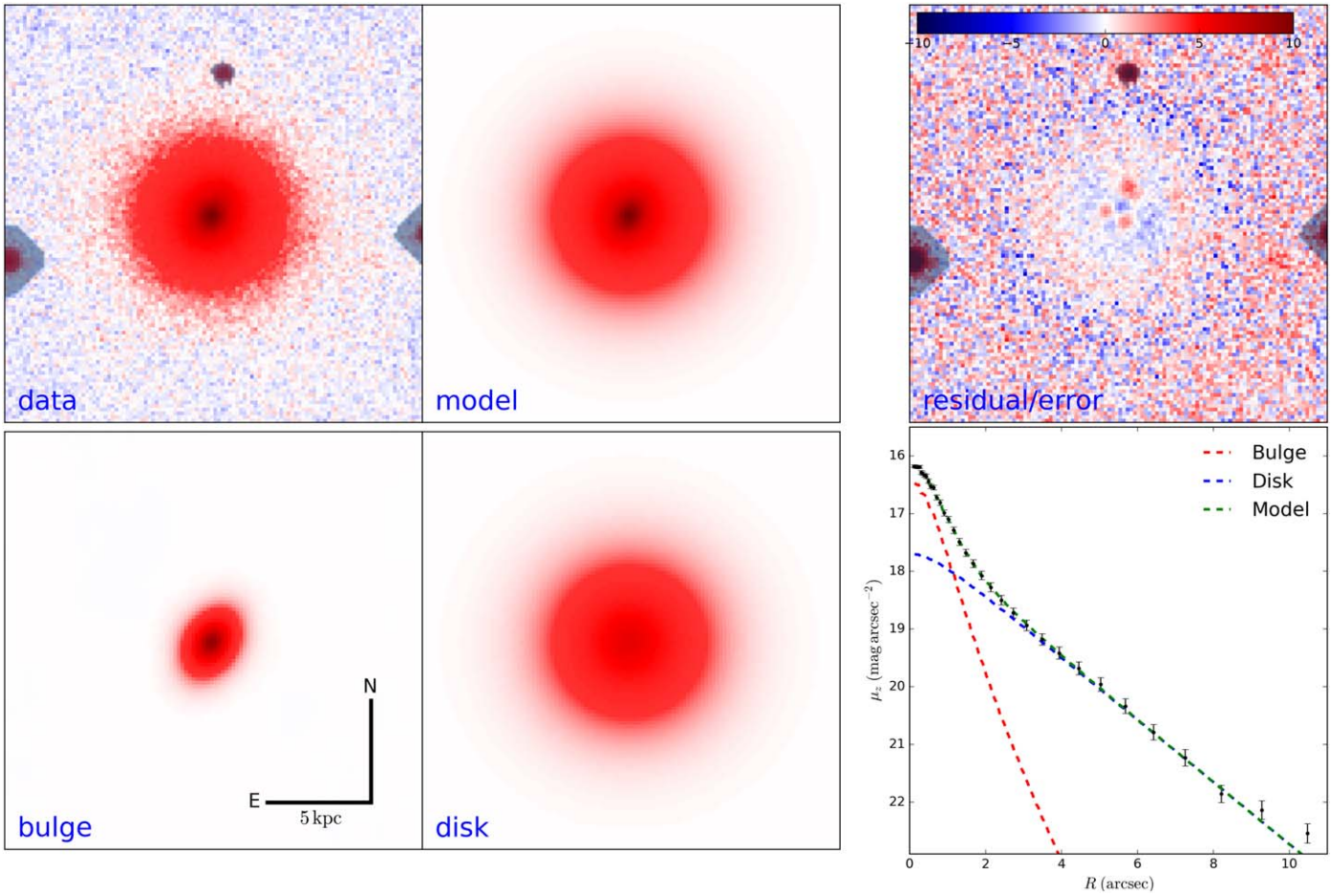


**Figure 2.** Results of the GALFITS imaging decomposition for the LS $z$-band image of AT2022lri's host galaxy. Upper left: The LS $z$-band image centered on AT2022lri, with a size of 30″. The shaded region represents a mask for contaminating sources. Upper middle: the model image generated using the best-fit GALFITS parameters detailed in Table 1. Upper right: the error-normalized residual image, obtained after subtracting the best-fit GALFITS model. Lower left: the model image of the bulge component. Lower middle: the model image of the disk component. Lower right: the surface brightness profile of the observed $z$-band image (black error bars), the bulge model (red), the disk model (blue), and the total GALFITS model (green).

**Table 1**
Properties of the Host Galaxy

| Component | $\log M_*$ ($M_\odot$) | $n$ | $R_e$ (arcsec) | $q$ | PA (deg.) | SFR ($M_\odot$ yr$^{-1}$) | $t_0$ (Gyr) | $A_V$ (mag) | $Z$ ($Z_\odot$) |
|---|---|---|---|---|---|---|---|---|---|
| bulge | $8.97 \pm 0.04$ | $1.93 \pm 0.11$ | $0.87 \pm 0.03$ | $0.62 \pm 0.02$ | $-28.9 \pm 1.1$ | $<3 \times 10^{-5}$ | $1.08 \pm 0.02$ | $0.34 \pm 0.06$ | $0.40 \pm 0.12$ |
| disk | $9.46 \pm 0.03$ | $0.92 \pm 0.04$ | $3.63 \pm 0.05$ | $0.96 \pm 0.01$ | $-89.4 \pm 1.3$ | $<1 \times 10^{-4}$ | $1.41 \pm 0.02$ | $0.31 \pm 0.03$ | $0.20 \pm 0.06$ |

parameters. The morphological parameters are the Sérsic index ($n$), effective radius ($R_e$), axis ratio ($q$), and position angle (PA), where PA is measured counterclockwise from the north direction. For the SED, we assume the stellar populations consist of two parts: one single stellar population (a burst) and another with a constant star formation rate (SFR) since $z \simeq 15$. The SED's free parameters are the stellar mass ($M_*$) of the component, the age of the first stellar population ($t_0$), the SFR of the second stellar population, attenuation from dust in the $V$ band ($A_V$), and stellar metallicity ($Z$). GALFITS also considers the contribution from nebular emission to the SED. We fixed the gas phase metallicity to be the same as the stellar metallicity and set the ionization parameter $U = 10^{-3}$, which are tested to have negligible effects on the fitting. Nested sampling is used for posterior distribution estimation, where all parameters are assumed to have a uniform distribution, utilizing the PYTHON package `dynesty`. Based on our tests, the two-component model demonstrates a reduced chi-squared value of $\chi^2_r \simeq 0.33$, significantly better than that of the single-component model ($\chi^2_r \simeq 2.09$). The best-fit parameters from an analysis of 16 broadband images are shown in Table 1. The GALFITS model for the LS $z$-band image is shown as an example in Figure 2.

In Table 1, the first component has a larger Sérsic index ($n \simeq 1.93$) but a smaller size ($R_e \sim 0\farcs9$), while the second component has a Sérsic index of approximately 0.92 but a larger size ($R_e \sim 3\farcs6$). Consequently, we identify the first component as the stellar bulge and the second as the stellar disk. These components also exhibit notably different axis ratios; the disk component has $q \simeq 0.96$, suggesting a face-on view. Given that classical bulges typically have higher Sérsic indices than pseudo bulges (J. Kormendy & R. C. Kennicutt 2004; H. Gao et al. 2020), a bulge with $n \lesssim 2$ is usually indicative of a pseudo bulge (D. B. Fisher & N. Drory 2008). Additionally, pseudo bulges are often less spherical compared

to classical bulges (H. Gao et al. 2020). Therefore, the bulge of AT2022lri, with $n \simeq 1.93$ and $q \simeq 0.62$, is more likely to be a pseudo bulge.

### 2.3. Black Hole Mass

We infer the BH mass $M_{\rm BH}$ using host galaxy scaling relations. Notably, the velocity dispersion of $\sigma_* = 32.8 \pm 1.7\,{\rm km\,s^{-1}}$ (Section 2.1) measured for AT2022lri's host galaxy is lower than any of the 29 TDE hosts' $\sigma_*$ values summarized in the review article of K. D. French et al. (2020), and the 19 $\sigma_*$ measurements from the more recent ZTF sample by Y. Yao et al. (2023). To our knowledge, no other TDE host has been recorded with a lower measured velocity dispersion. Using the J. Kormendy & L. C. Ho (2013) $M_{\rm BH}$–$\sigma_*$ relation, we estimate $\log(M_{\rm BH}/M_\odot) = 5.05 \pm 0.25({\rm stat}) \pm 0.29({\rm sys})$. Using the J. E. Greene et al. (2020) $M_{\rm BH}$–$\sigma_*$ relation for late-type galaxies, we obtain $\log(M_{\rm BH}/M_\odot) = 4.61 \pm 0.42({\rm stat}) \pm 0.58({\rm sys})$. Using the L. Ferrarese & H. Ford (2005) $M_{\rm BH}$–$\sigma_*$ relation, we have $\log(M_{\rm BH}/M_\odot) = 4.40 \pm 0.36$.

The total stellar mass of the host is $\log(M_{\rm gal}/M_\odot) = 9.58 \pm 0.03$ (sum of the bulge and disk masses in Table 1). This is lower than 78% (29/37) of the TDE hosts' $M_{\rm gal}$ values in K. D. French et al. (2020), and lower than 85% (28/33) of $M_{\rm gal}$ measurements from Y. Yao et al. (2023). Using the J. E. Greene et al. (2020) $M_{\rm BH}$–$M_{\rm gal}$ relation for late-type galaxies, we obtain $\log(M_{\rm BH}/M_\odot) = 5.26 \pm 0.25({\rm stat}) \pm 0.65({\rm sys})$. Separately, using the bulge mass of $M_{\rm bulge} = 10^{8.97\pm0.04}\,M_\odot$ (Section 2.2) and the $M_{\rm BH}$–$M_{\rm bulge}$ correlation for pseudo bulges (J. Kormendy & L. C. Ho 2013; R. Li et al. 2022), we estimate $\log(M_{\rm BH}/M_\odot) = 5.88 \pm 0.05({\rm stat}) \pm 0.33({\rm sys})$.

To summarize, the $M_{\rm BH}$ values estimated from $\sigma_*$ are generally smaller[30] than that estimated using $M_{\rm gal}$ and $M_{\rm bulge}$. It is important to note that these estimations are influenced by inherent uncertainties in the scaling relations, which may stem from calibration uncertainty and increased dispersions at the low-mass end. In the following, we adopt an intermediate value of $\log(M_{\rm BH}/M_\odot) \approx 5$ while acknowledging that the uncertainty associated with this $M_{\rm BH}$ estimate can be as large as 1 dex.

### 2.4. Historical X-Ray Constraints

We obtained constraints on the historical X-ray luminosity of AT2022lri's host galaxy. The host was not detected by the ROSAT all sky survey (J. Trumper 1982; W. Voges et al. 1999) in 1990/1991 with a $3\sigma$ 0.1–2.4 keV upper limit of $<0.303\,{\rm count\,s^{-1}}$. Assuming an absorbed power-law spectral shape with Galactic $N_{\rm H}$ and $\Gamma = 2$, we obtain a 0.3–2 keV flux upper limit of $<2.3 \times 10^{-12}\,{\rm erg\,s^{-1}\,cm^{-2}}$. Assuming an absorbed blackbody spectral shape with Galactic $N_{\rm H}$ and $kT_{\rm bb} = 0.1$ keV gives a similar upper limit of $<2.1 \times 10^{-12}\,{\rm erg\,s^{-1}\,cm^{-2}}$.

On 2008 January 16, the field of AT2022lri was observed by Swift/XRT. We estimated a 0.3–10 keV $3\sigma$ upper limit of $4.80 \times 10^{-3}\,{\rm count\,s^{-1}}$. This corresponds to a 0.3–2 keV flux limit of $<7.0 \times 10^{-14}\,{\rm erg\,s^{-1}\,cm^{-2}}$ and $<1.1 \times 10^{-13}\,{\rm erg\,s^{-1}\,cm^{-2}}$ for a power-law and blackbody spectral shape, respectively.

To summarize, the host galaxy is X-ray faint, with a flux upper limit of $\lesssim 10^{-13}\,{\rm erg\,s^{-1}\,cm^{-2}}$, which corresponds to a luminosity upper limit of $\lesssim 2.5 \times 10^{41}\,{\rm erg\,s^{-1}}$. This further suggests that the host of AT2022lri does not contain an AGN, consistent with the lack of diagnostic AGN forbidden lines (such as [O III] and [N II]) in the very late-time optical spectra (see Section 3.4).

[30] This difference is possibly caused by a velocity dispersion drop in the central region of the host, which is not uncommon in S0 galaxies or galaxies in the mass bin of $9.5 < \log(M_{\rm gal}/M_\odot) < 10.0$ (N. N.-Q. Ouellette et al. 2022).

## 3. UV–Optical Observations and Analysis

### 3.1. Optical Photometry

We obtained ZTF and ATLAS forced photometry (J. L. Tonry et al. 2018; F. J. Masci et al. 2019; K. W. Smith et al. 2020; L. Shingles et al. 2021) using the median position of all ZTF alerts up to MJD 59940. For ZTF data, we performed baseline correction and applied quality cuts following the procedures outlined in Y. Yao et al. (2019). For ATLAS data, we cleaned and corrected the photometry using the `ATClean` method (S. Rest et al. 2024). The Galactic extinction-corrected optical light curves are shown in Figure 3, and presented in Appendix A (Table 5).

The forced ATLAS photometry reveals a $10\sigma$ detection on 2022 March 24 (MJD 59662.006) at $o = 17.92 \pm 0.11$ mag that precedes the ATLAS TNS report. This marks the first optical detection and the start of the TDE rise (see the inset of Figure 3). However, the peak of the optical light curve was missed due to Sun occultation. Fitting the first-year light curve with a Gaussian rise and a power-law decline yields a peak time around MJD 59682. Hereafter, we use $\delta t$ to denote rest-frame days relative to MJD 59682. We binned the optical light curves at $\delta t > 0$ by 1–14 days to reveal subthreshold optical detections at late time, and to facilitate SED modeling with the ultraviolet data (see details in Section 3.3).

### 3.2. Swift/UVOT Photometry

AT2022lri was observed by the Ultra-Violet/Optical Telescope (UVOT; P. W. A. Roming et al. 2005) on board Swift under a series of time-of-opportunity (ToO) requests submitted by Y. Yao.

UVOT observations were obtained with the "$U$+All UV" filters or the "All UV" filters. Some observations were split into two observation IDs (obsIDs). We stacked these adjacent obsIDs with `uvotimsum` to improve the sensitivity. The source flux was measured with `uvotsource`, using a circular region with $r_{\rm src} = 9''$. The relatively large radius was chosen to ensure the capture of all the host galaxy flux. The background flux was measured using four nearby circular source-free regions with $r_{\rm bkg} = 10''$. We estimated the host galaxy flux within a $9''$ aperture using a host galaxy synthesis model, which was constructed following the same procedures adopted by S. van Velzen et al. (2021) and E. Hammerstein et al. (2023). Figure 3 shows the host subtracted UVOT photometry. Our final UVOT photometry is presented in Appendix A (Table 5).

### 3.3. Modeling the UV and Optical Photometry

We modeled the UV and optical photometry of AT2022lri with a blackbody function following the method adopted by Y. Yao et al. (2020). We fitted for both the blackbody radius ($R_{\rm bb}$) and the blackbody temperature ($T_{\rm bb}$) for epochs where two conditions are met: (1) the number of filters with significant detections (signal-to-noise ratio, hereafter SNR, $> 3$) is greater than three, and (2) there is at least one significant detection in the optical (ZTF or ATLAS) band.

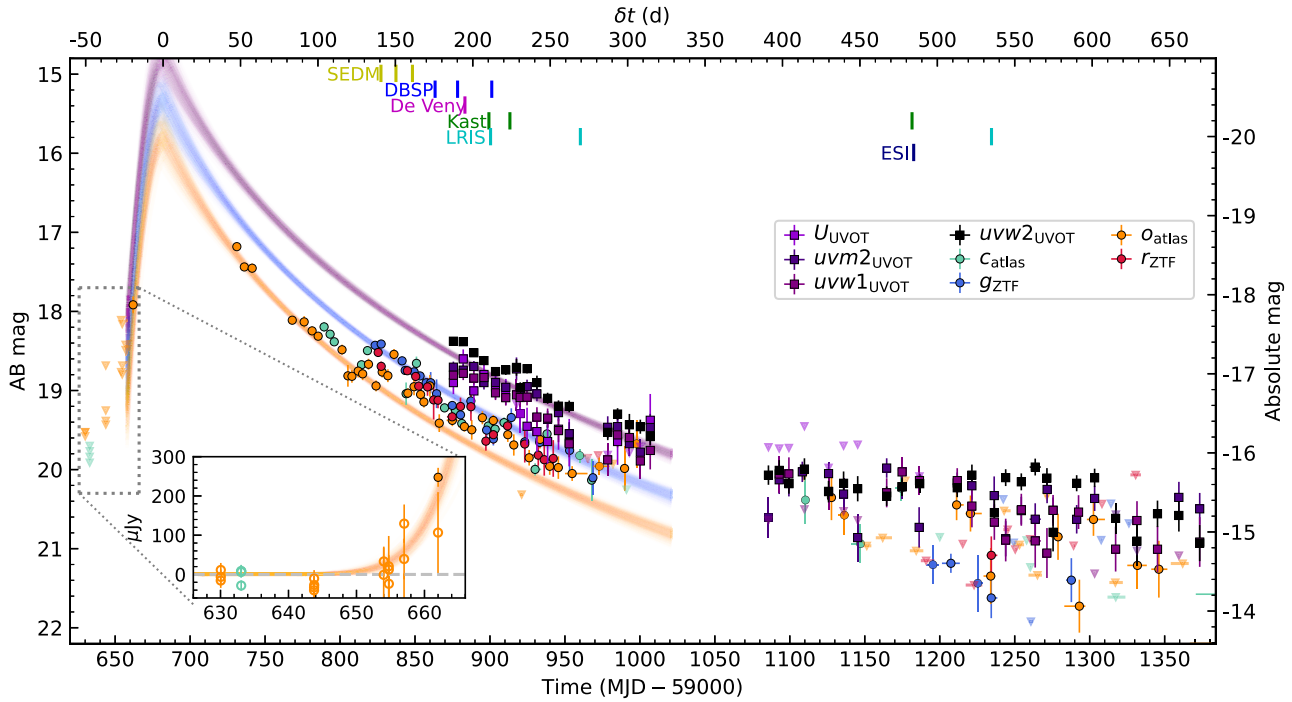


**Figure 3.** UV and optical light curves of AT2022lri. Solid points represent measurements above $3\sigma$, while semitransparent downward triangles show $3\sigma$ upper limits. The solid lines are single-temperature Gausssian-rise exponential-decline models in three bands ($o_{\rm ATLAS}$, $g_{\rm ZTF}$, and $uvw1_{\rm UVOT}$) fitted to the first-year data. The ticks along the upper axis marks the epoch of optical spectroscopy (Section 3.4). The inset shows the ATLAS light curve zoomed around time of first detection.

A total of 20 epochs met these conditions. For the remaining 23 epochs that do not satisfy the above conditions, we only fitted for $R_{\rm bb}$, while fixing the $T_{\rm bb}$ value to that of the closest epoch with a fitted $T_{\rm bb}$ estimate.

Generally speaking, the best-fit $T_{\rm bb}$ remains around $2.5\times10^4$ K, which is typical for ZTF-selected TDEs (E. Hammerstein et al. 2023; Y. Yao et al. 2023). The blackbody luminosity $L_{\rm bb}$ decreased from $\approx10^{43}$ erg s$^{-1}$ to $\approx10^{42}$ erg s$^{-1}$, and the blackbody radius $R_{\rm bb}$ decreased from $\approx2\times10^{14}$ cm to $\approx6\times10^{13}$ cm. These measurements are typical for optically selected TDEs (S. van Velzen et al. 2020; E. Hammerstein et al. 2023).

### 3.4. Low-resolution Optical Spectroscopy

Optical spectroscopic observations were coordinated in part with the `Fritz` platform (M. W. Coughlin et al. 2023) developed upon the `SkyPortal` software (S. van der Walt et al. 2019). Epochs of optical spectroscopy are marked along the upper axis of Figure 3.

We obtained low-resolution optical spectroscopy with the spectral energy distribution machine (SEDM; N. Blagorodnova et al. 2018; M. Rigault et al. 2019; Y. L. Kim et al. 2022) on the robotic Palomar 60 inch telescope (P60; S. B. Cenko et al. 2006), the DBSP on the Palomar 200 inch Hale telescope (P200), the De Veny Spectrograph on the Lowell Discovery Telescope (LDT), the Kast spectrograph on the Shane 3 m telescope at Lick Observatory (J. S. Miller & R. P. S. Stone 1993), and the Low Resolution Imaging Spectrograph (LRIS; J. B. Oke et al. 1995) on the Keck I telescope. A log is given in Appendix A (Table 6). Instrumental setup and data reduction of DBSP, De Veny, and LRIS spectra are the same as outlined in Appendix B of Y. Yao et al. (2022a). The Kast spectra used the D57 dichroic with the 600/4310 grism on the blue arm and the 300/7500 grating on the red side. The Kast reduction was performed in a similar manner to that outlined by J. M. Silverman et al. (2012). All low-resolution spectra are shown in the upper left panel of Figure 4.

To reveal weak TDE spectral features, we modeled the Kast and LRIS spectra at $\delta t<300$ days, as host-dominated spectra were available for these two instruments.[31] We modeled the observed spectra with a combination of blackbody continuum and host galaxy contribution: $f_{\lambda,\rm obs}=A_1f_{\lambda,\rm BB}+A_2f_{\lambda,\rm host}$, where $f_{\lambda,\rm BB}$ is obtained by using the best-fit blackbody parameters (Section 3.3), and $f_{\lambda,\rm host}$ is directly given by the late-time ($\delta t>480$ day) spectra. $A_1$ and $A_2$ are constants that account for unknown factors (see details in Section 4.2 of Y. Yao et al. 2022a). We searched for $A_1$ and $A_2$ that give the minimum $\chi^2$ in rest-frame 4000–7300 Å, while excluding the wavelength ranges that contain the Bowen complex (4500–4800 Å) and H$\alpha$ (6300–6700 Å).

The host and blackbody continuum subtracted spectra are shown in the lower left panel of Figure 4. While the Kast spectra do not show conclusive line features on the blue side (due to the low SNR), in the LRIS spectrum, intermediate-width emission lines around H$\beta$, the Bowen complex (He II $\lambda$4686 and N III $\lambda$4640), and possibly H$\gamma$ are clearly present. In addition, as shown in the upper left panel, a broad emission line around H$\alpha$ is evident in all observed spectra at $\delta t<300$ days. Using the classification scheme developed by S. van Velzen et al. (2021) and E. Hammerstein et al. (2023), the optical spectral subtype of AT2022lri belongs to the TDE-H+He subclass, which is the most common among optically selected TDEs.

The lower right panel of Figure 4 shows the H$\alpha$ profile in the host and continuum subtracted spectra. Fitting a Gaussian to each individual spectrum gives the measured full width at half-

[31] The +211.5 day LRIS spectrum was not included in this analysis as it was obtained with a different slit width from the +535.0 day LRIS observation, which resulted in mismatch in spectral resolution and host continuum shape.

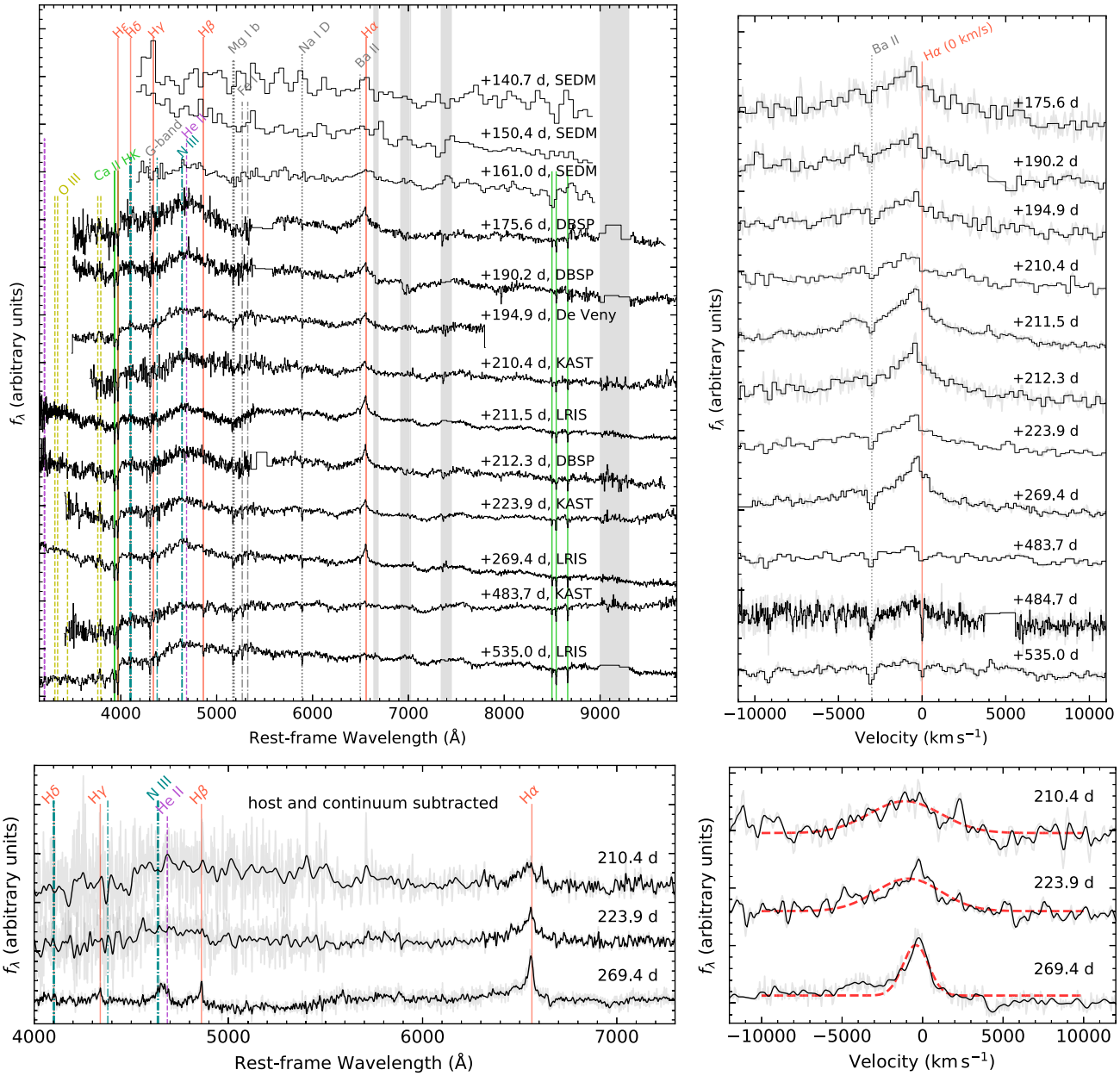


**Figure 4.** Upper left: Observed low-resolution optical spectra of AT2022lri. The vertical lines mark host galaxy lines and spectral lines common in TDEs. The gray bands mark atmospheric telluric features. Strong telluric features have been masked. Upper right: Zoom-in to the H$\alpha$ region of the observed spectra in velocity space. The ESI spectrum ($\delta t = 484.7$ days, Section 2.1) is also shown for comparison. Lower left: The translucent lines show host and continuum subtracted spectra, with the overlying black lines showing the same spectra convolved with Gaussian kernels for visual clarity. For the LRIS spectrum at +269.4 days, we use a kernel FWHM of 200 km s$^{-1}$. Since the Kast spectra are of lower SNR, we use FWHM kernel sizes of 1500 km s$^{-1}$ (1000 km s$^{-1}$) on the blue side at $\lambda_{\rm rest} \lesssim 6000$ Å, and 300 km s$^{-1}$ (200 km s$^{-1}$) on the red side for the +210.4 day (+223.9 day) data. Lower right: Zoom-in to the H$\alpha$ region of the host and continuum subtracted spectra in velocity space. The dashed red lines are Gaussian fits to the line profile.

maximum (FWHM) velocities (from +210.4 days to +269.4 days) of $5219 \pm 485$ km s$^{-1}$, $4763 \pm 309$ km s$^{-1}$, and $1887 \pm 95$ km s$^{-1}$, indicating that the H$\alpha$ line width becomes narrower at later times. The narrowing of optical lines is common in TDEs (S. van Velzen et al. 2020; P. Charalampopoulos et al. 2022). This might be caused by a drop of gas density in the line-forming region if the line width is mainly determined by electron scattering (N. Roth & D. Kasen 2018). The line centers are measured to be at $-1095 \pm 169$ km s$^{-1}$, $-887 \pm 111$ km s$^{-1}$, and $-425 \pm 38$ km s$^{-1}$. The slight blueshift by few $\times 10^2$ km s$^{-1}$ is also manifested in other spectra of AT2022lri shown in the upper right panel of Figure 4. We note that a blueshifted H$\alpha$ emission line has also been previously observed in other TDEs, albeit at much earlier times, such as in the peak-light spectra of ASASSN-14ae (T. W.-S. Holoien et al. 2014) and AT2018dyb (G. Leloudas et al. 2019). The blueshifted H$\alpha$ centroid observed in AT2022lri might be related to wide-angle outflows at $\delta t > 200$ days (N. Roth & D. Kasen 2018).

## 4. X-Ray Observations and Analysis

In this section, we conduct a detailed analysis of the X-ray observations of AT2022lri, focusing on its spectral properties.

Section 4.1 offers a general introduction and the motivation behind the six main spectral components explored in this study. The technical details are provided in Sections 4.2–4.4, which can be skimmed by readers who are not interested in the specifics. The key X-ray results are summarized at the beginning of Section 5.

### 4.1. An Overview

X-ray data reduction was performed using `HEASoft` version 6.32.1, which contains the NICER Data Analysis Software (`nicerdas`) version 11a. X-ray spectral modeling was conducted with the `xspec` software (K. A. Arnaud 1996). For all spectral fits, we include the Galactic absorption using the `tbabs` model (J. Wilms et al. 2000), with the hydrogen-equivalent column density $N_{\rm H}$ fixed at $1.60 \times 10^{20}\,{\rm cm}^{-2}$ (HI4PI Collaboration et al. 2016). We also convolve all TDE spectral models with `zashift` to account for host redshift. All fitting is performed with $\chi^2$ statistics.

In Section 4.2, we analyzed the Swift/XRT data, where the typical number of net counts per spectrum is 300–1000. We found that the data could be well described by two simple continuum models commonly used in TDE X-ray spectral modeling (R. Saxton et al. 2020):

1. A multitemperature disk (`diskbb`; K. Makishima et al. 1986) assumes an optically thick, geometrically thin disk, where the effective temperature varies as a function of radius as $T(r) \propto r^{-3/4}$. The range of temperatures results in a broader spectrum compared to a single-temperature blackbody. The model is determined by two parameters: the inner disk temperature $T_{\rm in}$, and a normalization term ${\rm norm}_{\rm diskbb}$. The latter can be easily converted to $R_{\rm in}^{*} \equiv R_{\rm in}\sqrt{\cos i}$, where $R_{\rm in}$ is the inner disk radius, and $i$ is the system's inclination.
2. An empirical power law (`powerlaw`) effectively fits the hard-excess in high-quality TDE spectra. This model is characterized by two parameters: the power-law photon index $\Gamma$, and a normalization term ${\rm norm}_{\rm PL}$.

In Section 4.3, we analyzed the data from the XMM-Newton telescope, which has two X-ray instruments: the European Photon Imaging Camera (EPIC) with the pn (L. Strüder et al. 2001) and MOS chips, and the Reflection Grating Spectrometer (RGS; J. W. den Herder et al. 2001). The EPIC/pn spectra, with a typical number of net counts of $\sim 10^5$, reveal additional spectral residuals around 1 keV that are not captured by continuum models like `diskbb`and `powerlaw`.

3. A single Gaussian spectral line (`Gaussian`) is added to account for the $\sim$1 keV residuals. This is motivated by the observation of a similar spectral feature in the super-Eddington flow of the X-ray transient 1ES 1927+654 (see Section 5.2.3 for a detailed comparison with this object), which C. Ricci et al. (2021) modeled using a Gaussian emission line. This model is defined by three parameters: the line center $E_{\rm line}$, the line width $\sigma_{\rm line}$, and a normalization term ${\rm norm}_{\rm gaus}$.

In Section 4.4, we analyzed the NICER data. While the model used to fit the EPIC/pn spectra generally provided a reasonable fit, we observed that the 1 keV residual feature did not appear to be symmetric in some NICER observations, especially during the X-ray dips. To address this, we further explored two physically motivated models. First, we consider absorption of continuum emission by an ionized outflow (`outflow_abs`) as well as emission from the outflow itself (`outflow_emi`):

4. The choice of `outflow_abs` was motivated by the similarity of the residuals below $\sim$1 keV (e.g., a flux excess around 0.5–0.6 keV and a flux deficiency around 0.7–0.8 keV) to those observed in two previously known X-ray bright TDEs, ASASSN-14li and AT2020ksf. The X-ray spectra of both events have been modeled with absorption from blueshifted, ionized outflows (E. Kara et al. 2018; Y. Ajay et al. 2024; T. Wevers et al. 2024). The `outflow_abs` model has three free parameters: the hydrogen column density of the ionized absorber $N_{\rm H,out}$, the ionization parameter $\xi$, and the redshift of the absorber $z_{\rm abs}$.[32]
5. In AT2022lri, the broader NICER spectral energy ranges reveal that the residuals are even stronger at 1–2 keV. We find that, when modeled with an ionized absorber, emission from the ionized material is further required. The `outflow_emi` model has five parameters. The first two parameters, $N_{\rm H,\ out}$ and $\xi$, are tied to those in the `outflow_abs` component. The other three parameters are the redshift of the emission component $z_{\rm emi}$, a normalization term ${\rm norm}_{\rm emi}$, and the line-broadening factor $\sigma_{\rm emi}$ that accounts for the integration of emission through the outflow geometry.

Next, we consider a recently developed reflection model for fitting the X-ray spectra of TDEs.

6. This reflection model (`reflTDE`) was first introduced in M. Masterson et al. (2022) to fit the high-quality spectra of 1ES 1927+654. It considers emission from a geometrically thick disk (approximated by a blackbody illumination spectrum) off an ionized slab. The model has eight free parameters: the blackbody temperature $kT_{\rm bb}$, the iron abundance with respect to its solar value $A_{\rm Fe}$, the ionization parameter at the surface of the disk $\xi$, the gas density $n$, the inclination $i$, the redshift $z_{\rm refl}$ of the slab materials that reprocess the irradiation continuum, a normalization term ${\rm norm}_{\rm refl}$, and the line-broadening factor $\sigma_{\rm refl}$ that accounts for velocity broadening.

### 4.2. Swift/XRT

All XRT observations were obtained in the photon-counting mode. Using an automated online tool[33] (P. A. Evans et al. 2007, 2009), we generated the light curve (0.3–1.5 keV; Figure 5) and spectra for all epochs. The spectra are further grouped with `ftgrouppha` using the optimal binning scheme (J. S. Kaastra & J. A. M. Bleeker 2016) and simultaneously ensure at least 25 counts per bin.

Since the XRT spectra remain soft, we first fit the data with `diskbb`, considering the energy ranges between 0.3 keV and wherever the net count rate becomes less than 1.5 times the background count rate. While some of the initial spectra can be well described by a multitemperature disk, at later epochs, the values of $\chi^2$/degrees of freedom (dof) become large, leaving a

[32] Throughout the rest of this paper, instead of reporting redshift, we report the outflow velocity inferred using the relativistic Doppler formula, $1 + z = \sqrt{(1 + v/c)/(1 - v/c)}$.

[33] https://www.swift.ac.uk/user_objects

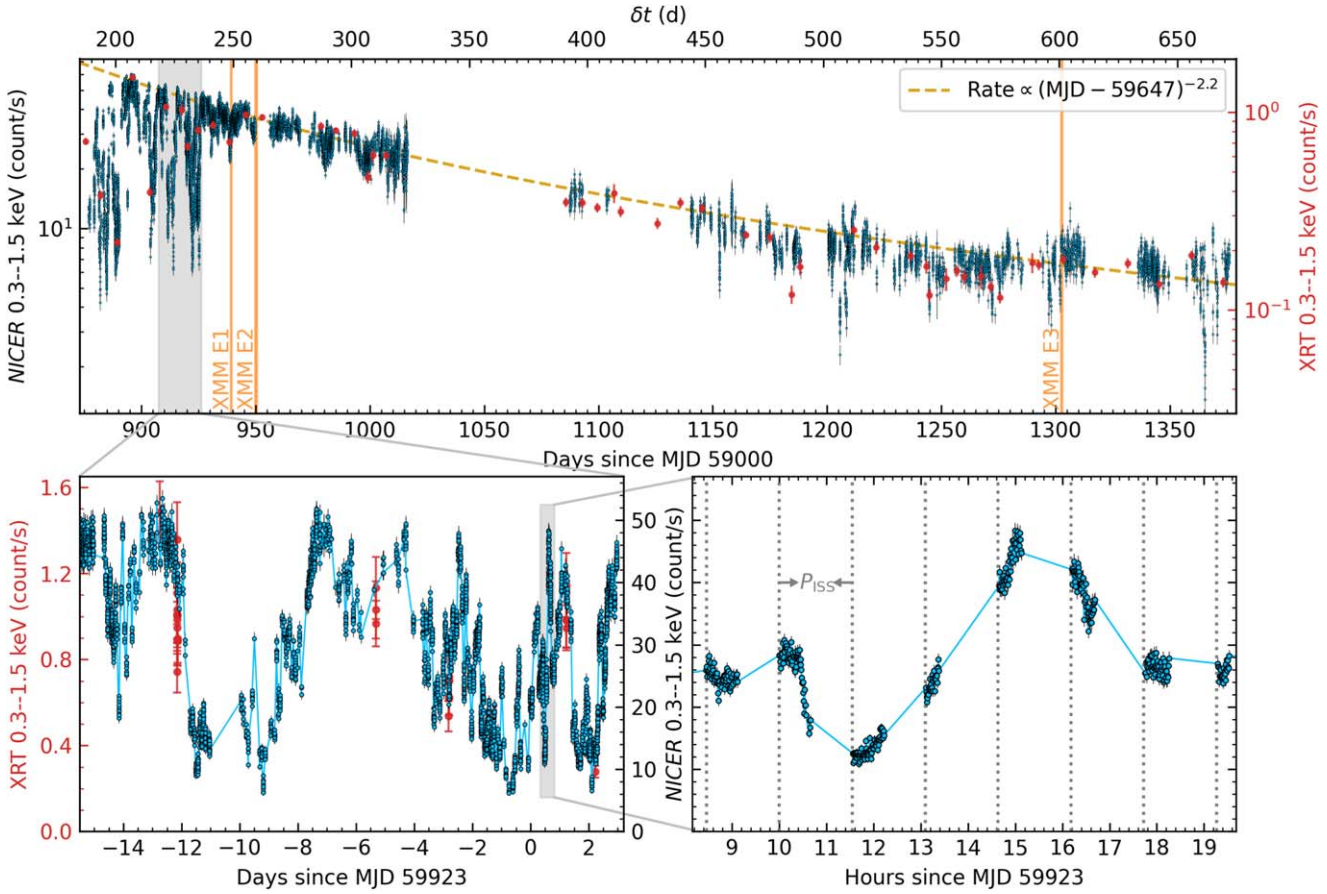


**Figure 5.** X-ray light curve of AT2022lri. Upper: The vertical orange bands mark three epochs of XMM-Newton observations. The dashed yellow line shows a power-law decline to guide the eye. Lower: A zoom-in around MJD 59923 to highlight the variability timescale at $t_{\rm var} \sim 1$ hr. The vertical dotted lines in the lower right panel mark the beginning of each GTI.

hard excess unaccounted for by the model. This suggests the existence of nonthermal Comptonized X-ray photons. Therefore, we remodeled the XRT spectra by adding a `powerlaw` component, which significantly improved the fit. If we let $\Gamma$ be a free parameter, we find that $\Gamma$ can only be constrained in $\sim$20% of XRT observations, where the best-fit $\Gamma$ ranges from 2.3 to 3.4, with a median at 2.8. However, even in these observations, the fractional uncertainties are typically greater than 50%. Therefore, we refitted the spectra with $\Gamma$ fixed at 2.8. The resulting $\chi^2$/dof is close to 1 in most of the cases.

In Figure 6, we show the unabsorbed rest-frame 0.3–2 keV X-ray luminosity $L_{0.3-2,\rm unabs}$ (panel (b)), the ratio of 0.3–2 keV fluxes in the `powerlaw` to `diskbb` components $f_{\rm PL}/f_{\rm diskbb}$ (panel (c)), $T_{\rm in}$ (panel (e)), $R_{\rm in}^*$ (panel (f)), and the $\chi^2$/dof values (panel (g)).

### 4.3. XMM-Newton

We obtained three epochs of observations with the XMM-Newton telescope (indicated by the vertical orange lines in Figure 5) through our GO and Directors Discretionary Time (DDT) programs. An observing log is given in Appendix A (Table 7).

#### 4.3.1. EPIC Analysis

Standard reduction procedures for the EPIC camera were employed, as detailed in M. Guolo et al. (2024). Prior to extracting X-ray spectra, we had to account for effects of photon pileup, which is prevalent in soft sources with high X-ray flux.

For the XMM E1 observation performed in the "Full Frame" mode, the pileup was so extreme that even excluding a large portion of the PSF did not correct all the pileup spectral distortions. We therefore decided to not use the EPIC data for this observation.

The XMM E2 and XMM E3 observations were performed in the "Small Window" mode, and pileup correction is feasible. In both observations, we considered an annular source region with a fixed outer radius of 32″ centered on the source coordinates. After quantifying the pileup by following the procedure outlined on XMM-Newton's data analysis page,[34] we selected inner exclusion radii of 11″ for XMM E2 and 3″ for XMM E3. A circle with $r_{\rm bkg} = 45''$ outside the source area, but within the same CCD, was chosen to generate the background spectrum. Using the `evselect` task, we only retained patterns that correspond to single events. Since the pileup was even more extreme in MOS1 and MOS2, and that the pn instrument has better sensitivity, we only analyzed the pn data. Both spectra were binned using the optimal binning criteria (J. S. Kaastra & J. A. M. Bleeker 2016) while ensuring that each bin has at least 25 counts.

Figure 7 shows the 50 s binned light curve of the XMM E2 and XMM E3 observations. In XMM E2, no strong variability

[34] https://www.cosmos.esa.int/web/xmm-newton/sas-thread-epatplot

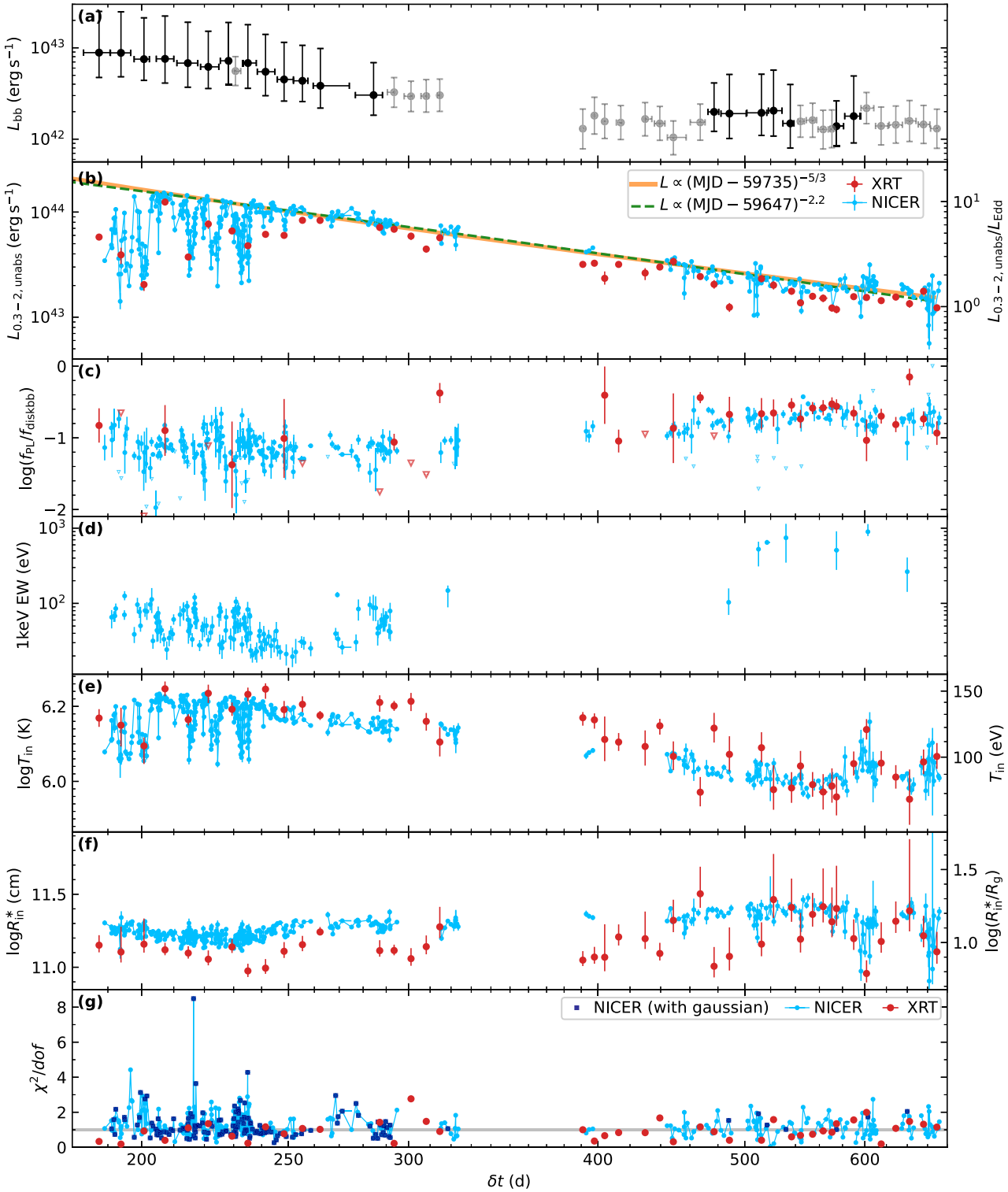


**Figure 6.** Multiwavelength evolution of AT2022lri. Panel (a): blackbody luminosity of the UV/optical emission. Black circles mark epochs where both $T_{\mathrm{bb}}$ and $R_{\mathrm{bb}}$ are fitted, while gray circles mark epochs where only $R_{\mathrm{bb}}$ is fitted (see details in Section 3.3). Panel (b): the unabsorbed rest-frame 0.3–2 keV X-ray luminosity. Panel (c): the ratio of the 0.3–2 keV `powerlaw` to `diskbb` fluxes. Panel (d): equivalent width (EW) of the 1 keV line, only shown if the model fit with the `Gaussian` component is favored with the BIC criterion (see details in Section 4.4.2). Panel (e)–(f): best-fit $T_{\mathrm{in}}$ and $R^*_{\mathrm{in}} \equiv R_{\mathrm{in}}\sqrt{\cos i}$ in the `diskbb` component. Panel (g): fit statistics. In the right $y$-axis of panels (b) and (f), we assume $M_{\mathrm{BH}} = 10^5\,M_\odot$ (see Section 2.3).

was observed. While in XMM E3, we observe a flux variation by a factor of ≈3.7 within ≈44 minutes.

For EPIC spectral fitting, we consider data between 0.3 keV and wherever the net count rate becomes less than 1.5 times the background count rate, which gives 2.2 keV for XMM E2 and 2.1 keV for XMM E3. Since a combination of `diskbb` and `powerlaw` provides acceptable fits to the XRT data (Section 4.2), we started from this continuum model, allowing $T_{\mathrm{in}}$, $R^*_{\mathrm{in}}$, $\Gamma$, and $\mathrm{norm}_{\mathrm{PL}}$ to be free parameters. In both observations, we obtained poor fits, with $\chi^2/\mathrm{dof} = 48.34/25$

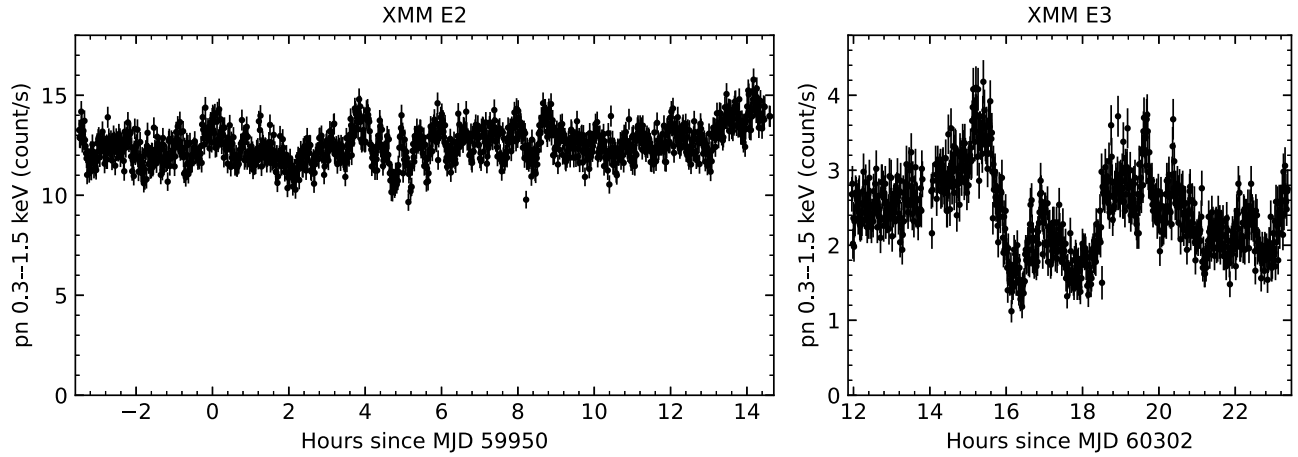


**Figure 7.** XMM-Newton/EPIC light curve of AT2022lri in the second (left) and third (right) epochs. Bins with background flaring have been masked out.

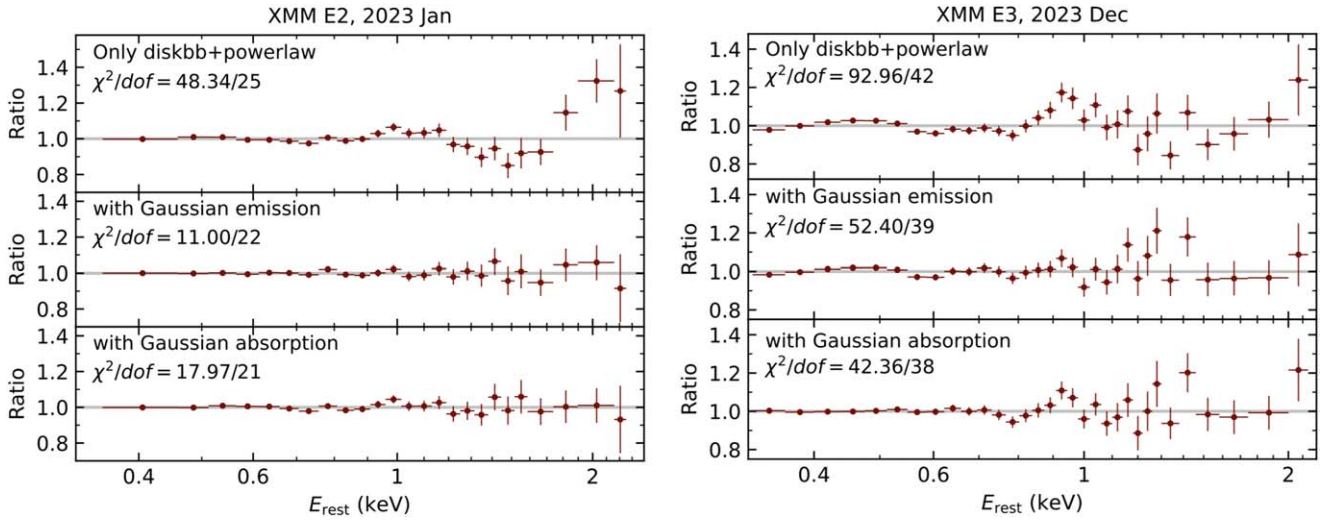


**Figure 8.** Ratio of the XMM E2 (left) and XMM E3 (right) EPIC/pn data fit to various models.

in XMM E2 and $\chi^2/\mathrm{dof} = 92.96/42$ in XMM E3 (see Figure 8, top rows). Changing the `diskbb` component to other thermal models such as `tdediscspec` (A. Mummery 2021) and `bbody` or changing the `powerlaw` component to other Comptonization models such as `simpl` (J. F. Steiner et al. 2009) or `cutoffpl` do not fit the residual.

To improve the fit, we first tried adding a `Gaussian` emission component, allowing $E_{\mathrm{line}}$ to vary between 0.8 and 1.2 keV and $\mathrm{norm}_{\mathrm{gaus}}$ to be positive. This significantly improved the fits (see Figure 8, middle rows). The best-fit $E_{\mathrm{line}}$ is capped at the minimum value of 0.8 keV in XMM E2, and $E_{\mathrm{line}} = 0.90^{+0.03}_{-0.04}$ keV in XMM E3.

Alternatively, we also tried adding a `Gaussian` absorption component, allowing $E_{\mathrm{line}}$ to vary between 1.0 and 1.8 keV and $\mathrm{norm}_{\mathrm{gaus}}$ to be negative. In this scenario, we found that the models systematically overpredict the flux at $\lesssim$0.4 keV. Therefore, we added an additional component of neutral absorption (`tbabs`) at the host redshift.

This also gives acceptable fits (see Figure 8, bottom rows). In XMM E2, the best-fit $E_{\mathrm{line}} = 1.35^{+0.05}_{-0.09}$ keV, and $N_{\mathrm{H,host}} = 1.46^{+0.64}_{-0.64} \times 10^{20}\,\mathrm{cm}^{-2}$. In XMM E3, the best-fit $E_{\mathrm{line}} = 1.16^{+0.09}_{-0.09}$ keV, and $N_{\mathrm{H,host}} = 2.80^{+0.52}_{-0.49} \times 10^{20}\,\mathrm{cm}^{-2}$.

Since the spectral residuals after adding an emission or absorption line are not particularly strong, we did not apply other physically motivated models to these observations.

#### 4.3.2. RGS Analysis

In the XMM E2 visit, the long exposure time and high X-ray flux of AT2022lri allowed for a high SNR RGS spectrum. Data reduction follows procedures adopted by J. M. Miller et al. (2015), which presented the RGS spectrum of the TDE ASASSN-14li. The `rgsproc` routine was used to generate RGS spectral files from the source, background spectral files, and instrument response files. The spectrum was binned by a factor of 5 for clarity.

We model the wavelength range where the net count rate is greater than 1.5 times the background count rate, which gives 9.9–37.3 Å. A combination of `diskbb` and `powerlaw` gives an acceptable fit, with $\chi^2/\mathrm{dof} = 591.39/532$. No strong absorption lines were evident in the RGS spectrum (see Figure 9). This suggests two possibilities: either there is no low-velocity outflow obscuring the inner disk, or the outflow's column density and ionization state are at levels where the lines

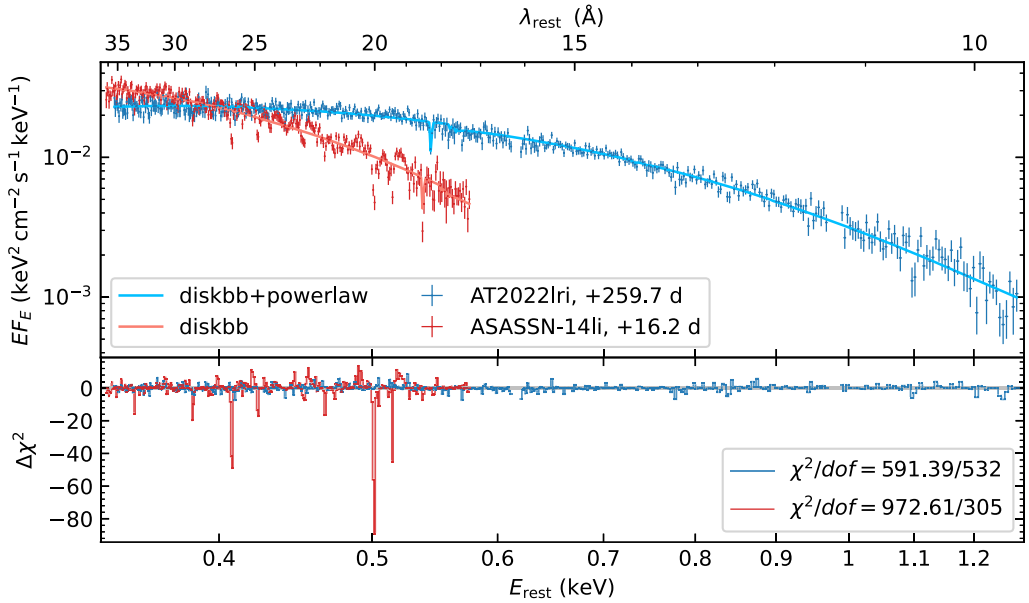


**Figure 9.** A comparison between the RGS spectrum of AT2022lri to that of ASASSN-14li (J. M. Miller et al. 2015). While strong narrow absorption lines were seen in ASASSN-14li, the spectrum of AT2022lri can be well described by the continuum model.

are too faint to be observed effectively. The potential presence of very weak lines is beyond the scope of this manuscript.

### 4.4. NICER

NICER is an X-ray telescope on the International Space Station (ISS), which has an orbital period of $P_{\rm ISS} = 92.9$ minutes. The X-ray timing instrument contains 56 X-ray "concentrators" (T. Okajima et al. 2016) and the associated focal plane module detectors. High-cadence NICER X-ray observations were obtained as part of our GO programs (PI: Y. Yao, IDs 5035, 6078; PI: T. Wevers, ID 6124). We note that, although the NICER GO program asked for a lower cadence (3 ks per 2 days), the NICER team increased the cadence based on initial quick look data.

Within the NICER field of view (FoV) of 30 arcmin$^2$, there exists no bright X-ray objects close to AT2022lri (see details in Appendix B.1). We processed the data with `nicerl2` following the standard pipeline.

#### 4.4.1. Light Curves

Using `nicerl3-lc`, we extracted light curves in the 0.3–1.5 keV range with a time bin of 32 s. The extracted light curves are normalized to an effective area with 52 detectors. Additional screening criteria were applied to improve the light-curve quality. First, we removed time bins with high background noise by requiring that the 13–15 keV (background dominated) count rate is less than 0.5 count s$^{-1}$. Next, we set the minimum acceptable fractional exposure to be 0.7 by removing time bins with `FRACEXP<0.7`. Finally, we found that some obsIDs were affected by local obstructions due to ISS hardware near the NICER FoV.[35] In our observations, such obscurations typically cause the egress (ingress) of a "dipping" behavior at the beginning (end) of certain good time intervals (GTIs). We visually inspected the light curves, and excluded dips at GTI edges that were associated with lower values of `ST_STARS` and `ST_OBJECTS` in the filter file.

The top panel of Figure 5 shows the NICER 0.3–1.5 keV light curve of AT2022lri. The light curve at $\delta t \lesssim 260$ days exhibits large-amplitude variability on top of a decaying trend, as indicated by the dashed yellow line. The lower panels of Figure 5 zoom-in around MJD 59923 to highlight the observed short-timescale X-ray variability. For the highest-cadence NICER observations (e.g., shown in the lower right panel), the separation between consecutive GTIs is $P_{\rm ISS}$. Intra-GTI variability is clearly observed. The flux can change by a factor of $\approx$2 in $\approx$30 minutes, by a factor of $\approx$5 in $\approx$0.5 day, and by a factor of $\approx$8 in $\approx$1 day.

We ran a periodicity search on the NICER light curve by computing the Lomb–Scargle (J. T. VanderPlas 2018) and the multiharmonic analysis of variance (MHAOV; A. Schwarzenberg-Czerny 1996) periodograms, using a frequency grid from 0.002 day$^{-1}$ to 3 day$^{-1}$. For the MHAOV method, we employed a Fourier series model of five harmonics. The periodograms were computed with both the full NICER light curve and subchucks of the light curve across the evolution. No significant periodicity aside from $P_{\rm ISS}$ or its harmonics was found.

#### 4.4.2. Basic Spectral Modeling

While most previous TDE analyses utilizing NICER data focused on the obsID-grouped spectra, we note that AT2022lri exhibits strong variability within some obsIDs. For example, the lower right panel of Figure 5 shows a subset of data within obsID 5535022401. In such cases, spectral properties derived from the obsID-grouped data might not provide appropriate characterization of the X-ray properties. This issue is more severe during phases where higher amplitude X-ray variability was observed.

To mitigate this effect, we selected time boundaries for each spectrum to ensure that (i) the fractional count rate variation within each spectrum is less than 30%, and (ii) GTIs separated beyond a gap of 2 days are divided into different spectra. The

[35] See details of this issue at https://heasarc.gsfc.nasa.gov/docs/nicer/analysis_threads/iss_obstruction/.

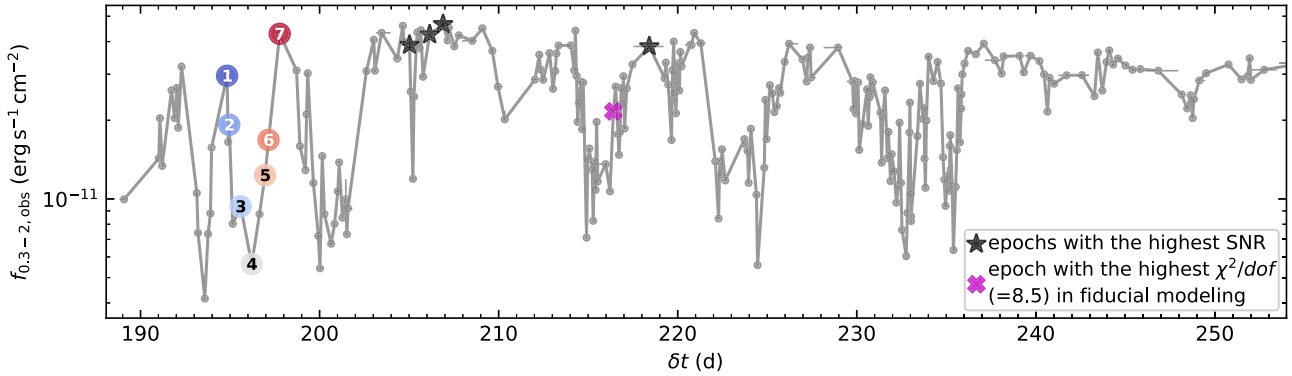


**Figure 10.** NICER observed 0.3–2 keV light curve of AT2022lri at $\delta t < 254$ days. The black asterisks mark four observations with high-quality data ($E_{\rm upper} > 2.1$ keV, net counts $> 5 \times 10^4$) selected for an initial basic spectral modeling. The magenta cross mark one observation selected for detailed modeling (see Figure 12). The large circles mark the assigned indices of seven observations during one X-ray dip (see Figure 13).

time files were created with `maketime`. Event filtering and spectral extraction were then performed with `niextract-events` and `nicerl3-spect`, respectively. Background spectra were created with the `3c50` model (R. A. Remillard et al. 2022). By default, `nicerl3-spec` adds a systematic uncertainty of ∼1.5%. Using `ftgrouppha`, we grouped the spectra using the J. S. Kaastra & J. A. M. Bleeker (2016) optimal binning method and simultaneously ensure a minimum of 25 counts per bin.

A total of 479 time-resolved spectra were generated. We first determined the energy range for spectral fitting by requiring that the net count rate is above 1.5 times the background count rate. We capped the lower boundary ($E_{\rm lower}$) to be $\geqslant$0.25 keV and the upper boundary ($E_{\rm upper}$) to be $\leqslant$10.0 keV. Next, we removed spectra with high background levels, selected if the 3–8 keV net count rate is greater than 0.8 count s$^{-1}$ or if the 0.25–0.35 keV background count rate is greater than 0.5 count s$^{-1}$. We also discarded spectra where the number of spectral bins between $E_{\rm lower}$ and $E_{\rm upper}$ is less than eight. A total of 429 spectra survived these cuts.

To obtain a general sense of the NICER spectral shape, we first looked at four spectra with the highest SNR by selecting those with broad energy ranges ($E_{\rm upper} > 2.1$ keV) and total net counts $>5 \times 10^4$ (see the black asterisks in Figure 10). We found that in all four observations, when fitted with a combination of `diskbb` and `powerlaw`, there exist residual features, which can be modeled with either an emission line at ∼1 keV or an absorption line at ∼1.3 keV, similar to what was found in the EPIC spectra (see Section 4.3.1).

For the purpose of a simple phenomenological modeling, we then decided to fit all time-resolved NICER spectra with two models (1) `tbabs*zashift*(powerlaw+diskbb)`, and (2) `tbabs*zashift*(Gaussian+powerlaw+diskbb)`, where $\sigma_{\rm line}$ and norm$_{\rm gaus}$ (forced to be positive) are allowed to be free, and $E_{\rm line}$ is fixed at 1 keV. The fact that $E_{\rm upper} \sim 1$ keV in most NICER spectra precludes constraints on the shape of the hard component. Therefore, in both models, we fixed $\Gamma$ at 2.8. We assess the goodness of fit by computing the model Bayesian information criterion (BIC): BIC $= k \cdot \ln(N) - 2\ln\mathcal{L} = k \cdot \ln(N) + \chi^2 +$ constant, where $k$ is the number of free parameters, $N$ is the number of spectral bins, and $\mathcal{L}$ is the maximum of the likelihood function. Following the A. E. Raftery (1995) guidelines, we select the fitting results from model (2) if its BIC value is more than 6 smaller than that in model (1).

The fitting results are presented in Figures 6 and 11. The evolution of $L_{0.3-2,\rm unabs}$ shows short-timescale dips on top of a general long-term declining trend, which we call the "envelope" of the X-ray light curve. Assuming that the "envelope" follows a power-law $\propto(t - t_{\rm disr})^{-\alpha}$, we found that the best-fit $t_{\rm disr} = 59735 \pm 3$ (in MJD) if $\alpha = 5/3$ and $t_{\rm disr} = 59647 \pm 4$ if $\alpha = 2.2$. We adopt the fit with $\alpha = 2.2$ as the disruption epoch $t_{\rm disr}$ should precede the first optical detection epoch (see Figure 3 and Section 3.1).

Throughout the X-ray evolution, the inferred $R_{\rm in}^*$ parameter remains roughly constant at $\sim 2 \times 10^{11}$ cm. Both the long-term X-ray flux decline trend and the X-ray dips at $\delta t \lesssim 240$ days seem to be correlated with changes in the inner disk temperature $T_{\rm in}$. Fitting a function of the type $\log(L_{\rm diskbb}/{\rm erg\ s^{-1}}) = a + b \times \log(T_{\rm in}/{\rm K}) + \epsilon$ yields a slope of $b = 4.02 \pm 0.05$ and an intrinsic scatter of $\epsilon = 0.08$, as shown in the left panel of Figure 11.

In observations where model (2) is favored with the BIC criterion, we found that the equivalent width of the 1 keV emission lines varies between ≈20 eV and ≈800 eV (see panel (d) of Figure 6 and the middle panel of Figure 11). The line width follows 30 eV $\lesssim \sigma_{\rm line} \lesssim$ 200 eV (see the right panel of Figure 11).

As shown in the bottom panel of Figure 6, in some epochs, the selected model does not provide a fit with $\chi^2/{\rm dof} < 2$, indicating that additional spectral features (other than a flux excess with a Gaussian profile at 1 keV) are present in the data.

#### 4.4.3. Modeling Additional Spectral Features

To investigate the shape of additional spectral features, we first focused on one observation with the highest value of $\chi^2/{\rm dof}$ (=8.5) in the phenomenological spectral modeling (Section 4.4.2). With total net counts $= 7.5 \times 10^4$, this observation (MJD = 59905.498, marked with a magenta cross in Figure 10) has a high SNR.

As a start, we fit the data with our fiducial model, `tbabs*zashift*diskbb`. A hard `powerlaw` component was found to be unnecessary for this observation and was therefore not included. As shown in the bottom left panel of Figure 12, the fiducial model leaves significant residuals. Adding a `Gaussian` emission or absorption component substantially improves the fit, but neither gives $\chi^2/{\rm dof} < 3$.

We attempted to improve the fit by adding absorption component(s) on top of our fiducial continuum model. We began by implementing neutral absorption (i.e., `tbabs`) at the host redshift. The best-fit model did not improve the fit, with the best-fit $N_{\rm H}$ being close to zero. We also tried partial

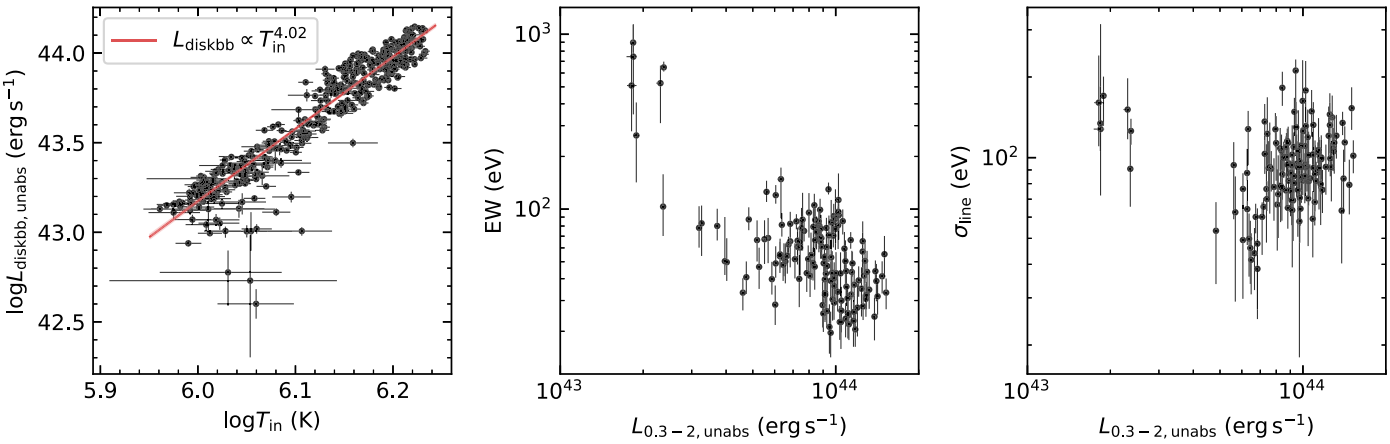


**Figure 11.** Model parameters in basic NICER spectral fitting. Left: $T_{\rm in}$ vs. the unabsorbed rest-frame 0.3–2 keV luminosity in the `diskbb` component. Middle: equivalent width of the 1 keV line vs. $L_{0.3-2,\rm unabs}$, only plotted for observations where the model fit with the `Gaussian` component is favored with the BIC criterion. Right: $\sigma_{\rm line}$ of 1 keV line vs. $L_{0.3-2,\rm unabs}$.

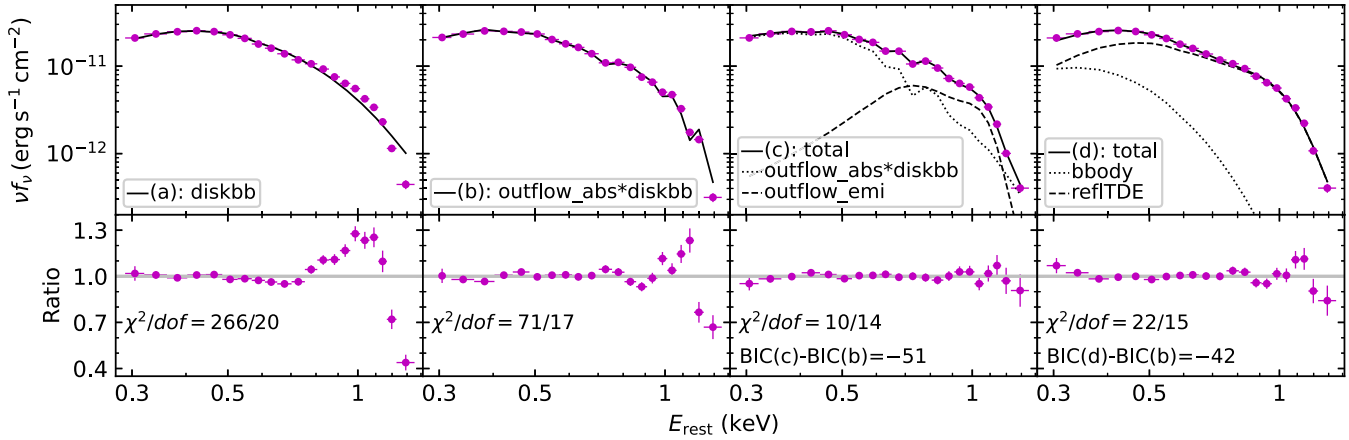


**Figure 12.** Spectral modeling results of the NICER observation on MJD 59905.498—the one with the highest $\chi^2$/dof in the initial analysis. From left to right, we show the data, best-fit models, and residuals under four different models. Models (c) and (d) give acceptable fits.

covering of neutral absorption (`pcfabs`), where a fraction of the X-ray source is seen through a neutral absorber, while the rest is assumed to be observed directly. This approach did not lead to an improved fit either.

Next, we tested the idea of absorption from an ionized absorber using `outflow_abs`. We performed photoionization absorption modeling using an absorption grid generated by `XSTAR` (T. Kallman & M. Bautista 2001), assuming an ionizing spectrum that follows the best-fit `diskbb+power-law` continuum at $\delta t = 218.4$ days when there was no X-ray dipping (i.e., $T_{\rm in} = 150$ keV, $\Gamma = 3.5$, shown as a black asterisk in Figure 10). Given the relative breadth of the spectral features and the limited energy resolution, we generated a model grid with a turbulent velocity of $v_{\rm turb} = 10^4\,{\rm km\,s^{-1}}$. Applying `tbabs*zashift*outflow_abs*diskbb` does not fully account for the residuals, shown as model (b) in Figure 12.

After that, we investigated if the fitting results can be further improved by adding emission from the ionized absorbers by using a model of `tbabs*zashift*(outflow_abs*−diskbb+outflow_emi)`. Similar models have been applied to AGN (E. Nardini et al. 2015; F. Tombesi et al. 2015; M. Laurenti et al. 2021) and TDE (E. Kara et al. 2018). Here, `outflow_emi` is defined as `gsmooth*emi`, where `emi` is an `XSTAR` emission table calculated with the same parameters as for the absorption table. Note that $z_{\rm emi}$ can be different from $z_{\rm abs}$, because the geometry of the outflow influences it. For instance, for a spherically symmetric outflow, we would expect a P-Cygni profile with blueshifted absorption along the line of sight and broad redshifted emission due to the other parts of the outflow not along the line of sight. If there is a disk occulting the back outflow, we would expect both emission and absorption to be blueshifted, but with different shifts due to the fact that emission comes from different directions. Roughly, the width of the emission should be comparable to the absorption outflow velocity. The `gsmooth` component is added because for a wide-angle outflow we expect emission to come from different regions of the outflow, with different projections along our line of sight. The fitting result is shown as model (c) in Figure 12, which gives $\chi^2/{\rm dof} = 10.27/14$ and a BIC value much smaller than that of model (b). The best-fit parameters are $N_{\rm H,out} = 2.37^{+0.86}_{-0.61} \times 10^{21}\,{\rm cm^{-2}}$, $\log(\xi/{\rm erg\,cm\,s^{-1}}) = 2.98^{+0.17}_{-0.03}$, $v_{\rm abs}/c = -0.110^{+0.014}_{-0.013}$, $T_{\rm in} = 116.9^{+2.4}_{-2.7}$ eV, ${\rm norm_{diskbb}} = 20.75^{+2.86}_{-2.14} \times 10^3$, $\sigma_{\rm emi} = 0.089^{+0.008}_{-0.007}$ keV, $v_{\rm emi}/c = -0.134^{+0.010}_{-0.009}$, and ${\rm norm_{emi}} = 8.98^{+2.35}_{-1.42} \times 10^{-3}$. We conclude that the model with both emission and absorption from the wind is favored over the one with only absorption.

Additionally, we test the reflection model `reflTDE`, defined as `gsmooth*xillverTDE`. While classic reflection models

**Table 2**
Statistics of Various Models Fitted to the Seven Observations at $\delta t \sim 196$ days

| Index | Model | $\chi^2$/dof | ΔBIC |
|---|---|---|---|
| (A) | Fiducial model: `tbabs*zashift*continuum` | 265.13/115 | 0 |
| (B) | `tbabs*zashift*outflow_abs*continuum` | 151.01/106 | −70.2 |
| (C) | `tbabs*zashift*(outflow_abs*continuum+outflow_emi)` | 102.83/97 | −74.5 |
| (D) | `tbabs*zashift*(reflTDE+continuum)` | 111.20/104 | −80.8 |

**Note.** ΔBIC is the difference of BIC values between each model and model (A). In models (A), (B), and (C), `continuum=diskbb` for sp1–sp6, and `continuum=(diskbb+powerlaw)` for sp7. In model (D), `continuum=bbody` for sp1–sp6, and `continuum=(bbody+powerlaw)` for sp7.

(e.g., `xillver`, `xillverCP`; J. García & T. R. Kallman 2010; J. García et al. 2013) are suitable for AGN and low-mass BH binaries in the hard-state, the power-law irradiation continuum in these models does not apply to thermally dominated X-ray spectra. In `xillverTDE`, the continuum is defined by a single-temperature blackbody spectrum with $0.03\ \mathrm{keV} < kT_{\rm bb} < 0.3\ \mathrm{keV}$, appropriate for the inner regions of a geometrically thick disk in TDEs (M. Masterson et al. 2022). The multiplicative component `gsmooth` was added to account for velocity broadening, which was found to exhibit a more symmetric profile in super-Eddington accretion flows (L. L. Thomsen et al. 2022a).

We applied the reflection model of `tbabs*zashift*(reflTDE+bbody)`, fixing $A_{\rm Fe} = 1$ and $i = 45°$ (as in M. Masterson et al. 2022) since the fit is not sensitive to these parameters. We tied the blackbody temperature in the `reflTDE` and `bbody` components to be the same. The fitting result, with $\chi^2/\mathrm{dof} = 22.40/15$ and named as model (d), is shown in the right panel of Figure 12. The best-fit parameters are $kT_{\rm bb} = 67.3^{+3.8}_{-5.0}$ eV, $\mathrm{norm_{bb}} = 27.4^{+1.4}_{-1.8} \times 10^{-5}$, $\sigma_{\rm refl} = 0.145^{+0.004}_{-0.014}$ keV, $\log(\xi/\mathrm{erg\ cm\ s^{-1}}) = 3.47^{+0.01}_{-0.10}$, $\log(n/\mathrm{cm^{-3}}) = 17.99^{+0.01}_{-0.44}$, $v_{\rm refl}/c = -0.262^{+0.021}_{-0.028}$, and $\mathrm{norm_{refl}} = 19.0^{+12.1}_{-1.3} \times 10^{-13}$.

We conclude that both model (c) and model (d) give acceptable fits. According to BIC, for this observation, the reflection model is not favored over modeling with an ionized absorber.

#### 4.4.4. Modeling of an X-Ray Dip

To investigate the evolution of spectral parameters during the rapid X-ray variability, we then focused on data at $\delta t \sim 196$ days and selected seven observations (hereafter referred as sp1–sp7) that sample one X-ray dip for a detailed analysis (see Figure 10 for epochs of these observations). Another goal of this step is to verify if the absorption/emission and reflection models that provide acceptable fits in Section 4.4.3 can be applied in other observations. A summary of the fit statistics of our models is given in Table 2. Below, we describe the fitting procedures.

Before applying complex models, we first started by individually fitting the seven spectra with `tbabs*zashift*continuum`, where `continuum=diskbb` for sp1–sp6, and `continuum=(diskbb+powerlaw)` for sp7.[36] We allowed the disk temperature and disk normalization to be different across the seven epochs. We hereafter refer to this best-fit fiducial model ($\chi^2/\mathrm{dof} = 265.13/115 = 2.31$) as model (A), which provides a reference point for model comparison. The fitting result is shown in the top two panels of Figure 13.

Next, we applied the absorption model of `tbabs*zashift*outflow_abs*continuum`. Following model (A), we chose `continuum=diskbb` for sp1–sp6, and `continuum=(diskbb+powerlaw)` for sp7. We tied $\log\xi$ and $z_{\rm abs}$ to be the same and allowed $N_{\rm H,\ out}$ to vary across observations. The best fit, named as model (B), gives $\chi^2/\mathrm{dof} = 151.01/106 = 1.42$ and represents a significant improvement over model (A). However, the best-fit $v_{\rm abs} = -0.64 \pm 0.01c$, which is faster than the velocity of any ultrafast outflows reported in the X-ray literature (∼0.03–0.59$c$, F. Tombesi et al. 2010; G. Chartas et al. 2021), and the corresponding model (b) do not provide an acceptable fit in Section 4.4.3.

Following that, we added emission from the ionized absorber by using `tbabs*zashift*(outflow_abs*continuum+outflow_emi)`. We tied $\sigma_{\rm emi}$ and $z_{\rm emi}$ to be the same and allowed $\mathrm{norm_{emi}}$ to vary across observations. The best fit, named as model (C), has $\chi^2/\mathrm{dof} = 102.83/97 = 1.06$ and is shown in the middle two rows of Figure 13. The best-fit parameters are presented in Table 3. We see that $\log\xi$, $v_{\rm abs}$, $v_{\rm emi}$, and $\sigma_{\rm emi}$ are all similar to values found in model (c) (see Section 4.4.3). We note that the main resonant emission and absorption features in the soft X-ray band for an ionization parameter $\log\xi \approx 3$ would come from O VIII, Ne IX/Ne X, and Fe L. Given the high number of lines from this range of ionized species and the limited energy resolution of the detectors, the features would appear blended together.

Finally, we applied the reflection model of `tbabs*zashift*(reflTDE+continuum)`, where `continuum=bbody` for sp1–sp6, and `continuum=(bbody+powerlaw)` for sp7. We allowed $\mathrm{norm_{refl}}$ to be different across observations, and tied the other four free parameters in `reflTDE` ($\xi$, $n$, $z_{\rm refl}$, and $\sigma_{\rm refl}$) to be the same. The best fit, with $\chi^2/\mathrm{dof} = 111.20/104 = 1.07$, is named as model (D) and shown in the bottom two rows of Figure 13. The best-fit parameters are presented in Table 4. We see that the best-fit $\log n$, $\log\xi$, and $v_{\rm refl}$ are slightly different from the best-fit values of model (d) shown in Section 4.4.3.

The upper panels of Figure 14 illustrate the flux variation across the seven observations, highlighting contributions from various spectral components. In both model (C) and model (D), the total luminosity (shown by the blue asterisks) initially decreased by a factor of ≈5 from sp1 to sp4, and then increased by a factor of ≈7 from sp4 to sp7. In model (C), the fluctuations in total luminosity mainly stem from changes in the `diskbb` component. We note that, since the $N_{\rm H,out}$ is relatively small (between $3.7 \times 10^{20}\ \mathrm{cm^{-2}}$ and $3.6 \times 10^{21}\ \mathrm{cm^{-2}}$, Table 3), the 0.3–2 keV `diskbb` luminosity before absorption by the ionized absorber is only a factor of 1.02–1.18 greater than the orange crosses shown in the upper left panel. In model

[36] Since $E_{\rm upper} \leqslant 1.3$ keV for the first six observations, adding a `powerlaw` component to sp1–sp6 yields a $\mathrm{norm_{PL}}$ with a lower end of the 90% confidence interval that is consistent with zero.

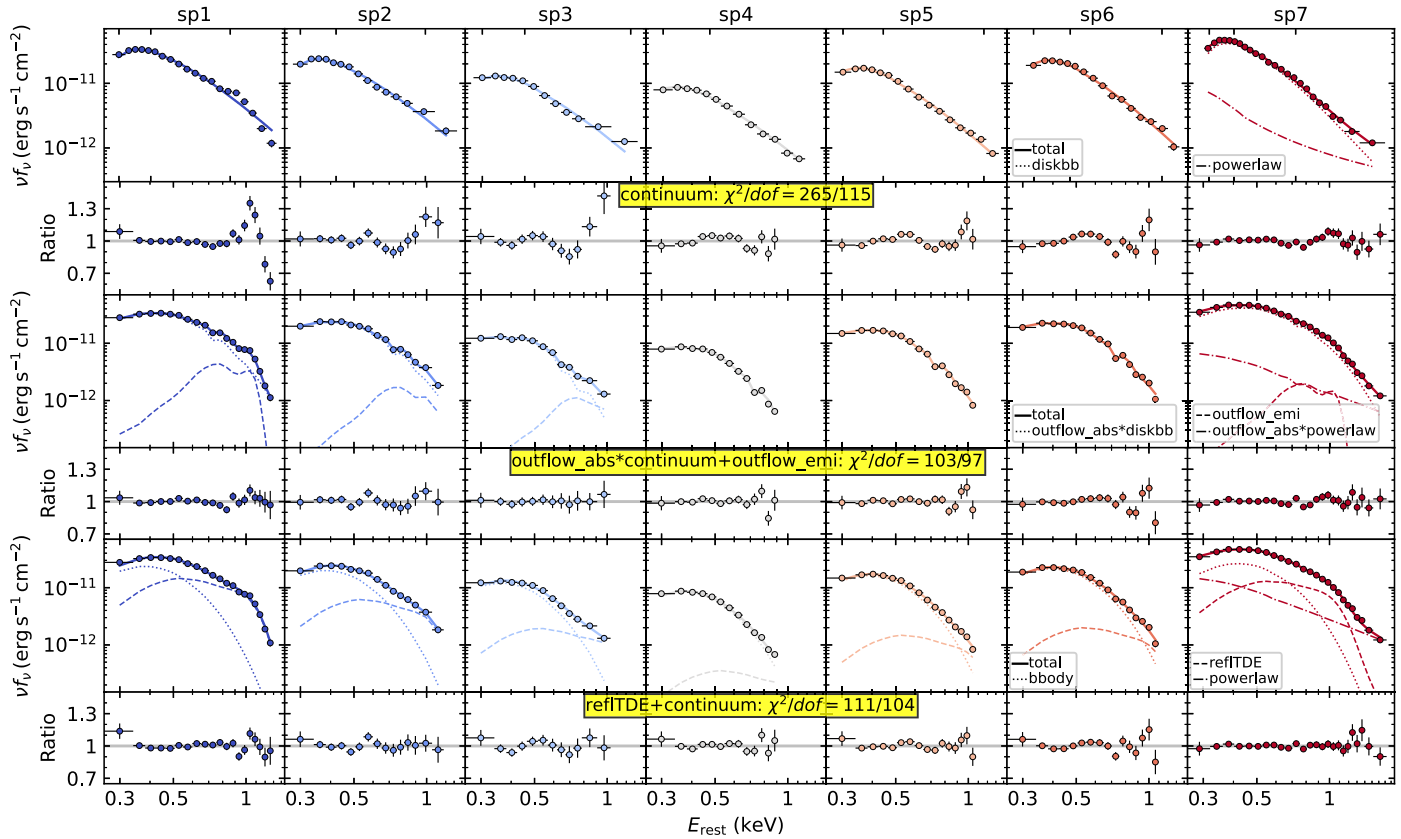


**Figure 13.** Seven observations around $\delta t \sim 196$ days jointly modeled with three different models. We show the data, best fits, and residuals for the fiducial continuum model (A) in the top two rows, the absorption+emission model (C) in the middle two rows (see Table 3 for the best-fit parameters), and the reflection model (D) in the bottom two rows (see Table 4 for the best-fit parameters).

**Table 3**
Model (C): Best-fit Parameters for Seven NICER Observation at $\delta t \sim 196$ days

| Component | Parameter | sp1 | sp2 | sp3 | sp4 | sp5 | sp6 | sp7 |
|---|---|---|---|---|---|---|---|---|
| outflow_abs | $N_{\rm H,out}$ ($10^{21}$ cm$^{-2}$) | $0.99^{+0.41}_{-0.14}$ | $1.28^{+0.62}_{-0.40}$ | $3.56^{+1.42}_{-1.07}$ | $1.45^{+0.24}_{-0.19}$ | $1.33^{+0.16}_{-0.15}$ | $1.36^{+0.18}_{-0.15}$ | $0.37^{+0.25}_{-0.14}$ |
| | log$\xi$ (erg cm s$^{-1}$) | | | | $3.00^{+0.06}_{-0.01}$ | | | |
| | $v_{\rm abs}/c$ | | | | $-0.110^{+0.010}_{-0.010}$ | | | |
| diskbb | $T_{\rm in}$ (eV) | $128.7^{+0.9}_{-2.3}$ | $120.8^{+1.2}_{-1.4}$ | $103.5^{+1.3}_{-1.3}$ | $102.3^{+0.9}_{-0.9}$ | $113.5^{+0.8}_{-0.7}$ | $117.9^{+0.8}_{-0.7}$ | $145.1^{+0.9}_{-2.0}$ |
| | norm$_{\rm diskbb}$ ($10^3$) | $16.74^{+0.11}_{-0.06}$ | $16.39^{+0.13}_{-0.12}$ | $20.97^{+0.18}_{-0.16}$ | $13.61^{+0.05}_{-0.06}$ | $16.02^{+0.04}_{-0.05}$ | $17.75^{+0.11}_{-0.06}$ | $11.94^{+0.04}_{-0.04}$ |
| powerlaw | $\Gamma$ | ... | ... | ... | ... | ... | ... | $3.66^{+0.10}_{-0.24}$ |
| | norm$_{\rm PL}$ ($10^{-5}$) | ... | ... | ... | ... | ... | ... | $97.0^{+9.6}_{-9.5}$ |
| outflow_emi | $\sigma_{\rm emi}$ (keV) | | | | $0.066^{+0.009}_{-0.008}$ | | | |
| | $v_{\rm emi}/c$ | | | | $-0.155^{+0.007}_{-0.007}$ | | | |
| | norm$_{\rm emi}$ ($10^{-3}$) | $25.42^{+2.32}_{-2.88}$ | $5.25^{+3.82}_{-1.44}$ | $1.17^{+0.23}_{-0.14}$ | $0.00^{0.08a}$ | $0.00^{0.16a}$ | $0.00^{0.17a}$ | $18.16^{+5.91}_{-3.42}$ |
| | $\chi^2$/dof | | | | 102.83/97 | | | |

**Notes.** Model (C): tbabs*zashift*(outflow_abs*continuum+outflow_emi), where continuum=diskbb for sp1–sp6, and continuum=(diskbb+powerlaw) for sp7.
[a] Parameter pegged at the minimum value of the model.

(D), the variability comes from variations in both the reflection component and the blackbody component.

The lower panels of Figure 14 show the temperature and radius evolution in the thermal components in each model. In model (C), $T_{\rm in}$ varies between $1.19 \times 10^6$ K and $1.68 \times 10^6$ K, and $R_{\rm in}^*$ experiences minor variations within the range of $(1.57\text{–}2.08) \times 10^{11}$ cm. Fitting a function of the type $\log(L_{\rm diskbb,\ unabs0}/{\rm erg\ s^{-1}}) = a + b \times \log(T_{\rm in}/{\rm K}) + \epsilon$ yields a slope of $b = 4.23^{+0.33}_{-0.52}$ and an intrinsic scatter of $\epsilon = 0.09$, where $L_{\rm diskbb,\ unabs0}$ is the 0.3–2 keV diskbb luminosity corrected for both Galactic absorption and absorption from the ionized absorber. In model (D), the blackbody temperature $T_{\rm bb}$ remains relatively constant at $(0.87\text{–}1.07) \times 10^6$ K, and the blackbody radius $R_{\rm bb}$ (inferred from the norm$_{\rm bb}$ parameter) changes within $(3.2\text{–}4.8) \times 10^{11}$ cm. Fitting a function of the type $\log(L_{\rm bbody,\ unabs}/{\rm erg\ s^{-1}}) = a + b \times \log(T_{\rm bb}/{\rm K}) + \epsilon$

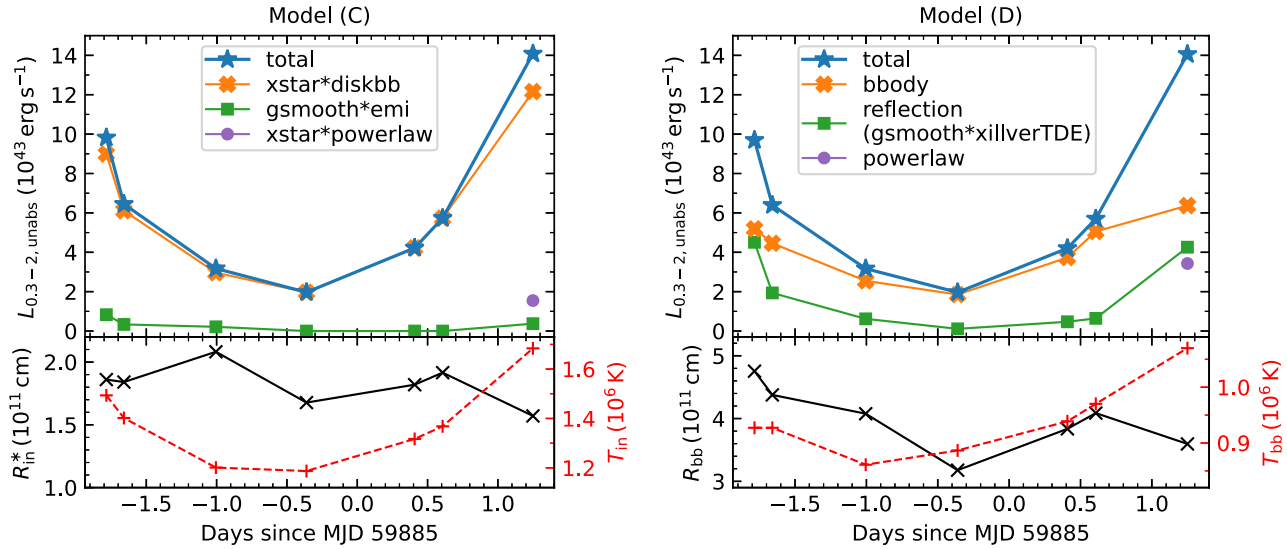


**Figure 14.** Upper: evolution of 0.3–2 keV X-ray luminosities in models (C) and (D), shown both in total and contributions in different spectral components. Lower: evolution of temperature ("+" connected by dashed lines) and radius ("×" connected by solid lines) in the `diskbb` component in model (C) and the `bbody` component in model (D).

**Table 4**
Model (D): Best-fit Parameters for Seven NICER Observation at $\delta t \sim 196$ days

| Component | Parameter | sp1 | sp2 | sp3 | sp4 | sp5 | sp6 | sp7 |
|---|---|---|---|---|---|---|---|---|
| `bbody` | $kT_{\rm bb}$ (eV) | $79.9^{+1.8}_{-2.7}$ | $79.9^{+1.9}_{-2.2}$ | $74.2^{+1.6}_{-1.6}$ | $76.4^{+1.1}_{-1.1}$ | $80.9^{+0.9}_{-0.9}$ | $83.6^{+1.2}_{-1.2}$ | $92.2^{+2.8}_{-5.4}$ |
| | norm$_{\rm bb}$ ($10^{-5}$) | $57.6^{+2.0}_{-3.6}$ | $48.8^{+1.4}_{-1.9}$ | $31.5^{+1.1}_{-1.0}$ | $21.5^{+0.4}_{-0.4}$ | $39.4^{+0.6}_{-0.6}$ | $51.0^{+0.8}_{-0.8}$ | $58.4^{+3.0}_{-7.2}$ |
| `powerlaw` | $\Gamma$ | ... | ... | ... | ... | ... | ... | $3.73^{+0.11}_{-0.08}$ |
| | norm$_{\rm PL}$ ($10^{-5}$) | ... | ... | ... | ... | ... | ... | $192.1^{+9.9}_{-12.2}$ |
| reflTDE | $\sigma_{\rm refl}$ (keV) | | | | $0.142^{+0.009}_{-0.007}$ | | | |
| | log$\xi$ (erg cm s$^{-1}$) | | | | $2.14^{+0.33}_{-0.02}$ | | | |
| | log$n$ (cm$^{-3}$) | | | | $19.00_{-0.91}$ [a] | | | |
| | $v_{\rm refl}/c$ | | | | $-0.340^{+0.013}_{-0.011}$ | | | |
| | $i$ (deg) | | | | 45 (frozen) | | | |
| | $A_{\rm Fe}$ | | | | 1 (frozen) | | | |
| | norm$_{\rm refl}$ ($10^{-13}$) | $21.8^{+38.7}_{-0.7}$ | $9.3^{+20.0}_{-1.2}$ | $2.9^{+8.4}_{-0.4}$ | $0.5^{+1.6}_{-0.2}$ | $2.2^{+6.3}_{-0.3}$ | $3.0^{+8.3}_{-0.6}$ | $19.6^{+54.3}_{-2.4}$ |
| | $\chi^2$/dof | | | | 111.20/104 | | | |

**Notes.** Model (D): `tbabs*zashift*(reflTDE+continuum)`, where `continuum=bbody` for sp1–sp6, and `continuum=(bbody+powerlaw)` for sp7.
[a] Parameter pegged at the maximum value of the model.

yields a slope of $b = 4.09^{+0.49}_{-0.62}$ and an intrinsic scatter of $\epsilon = 0.13$, where $L_{\rm bbody,\ unabs}$ is the 0.3–2 keV `bbody` luminosity corrected for Galactic absorption.

To summarize, both model (C) and model (D) provide good and statistically comparable fits to the observations. A few sanity checks were performed on these models (see details in Appendix B.2). We further discuss the implications of the fitting results in Section 5.1.3.

## 5. Discussion

Before delving into the physical interpretation of AT2022lri, we summarize the key X-ray results from Section 4.

1. We analyzed X-ray observations of AT2022lri spanning from $\delta t \sim 190$ days to $\delta t \sim 680$ days. The X-ray spectrum remains soft, and to a first approximation, the continuum can be described by a phenomenological model comprising a `diskbb` and a `powerlaw` component.
2. From $\delta t \sim 190$ days to $\delta t \sim 570$ days, the ratio of the 0.3–2.0 keV flux in the `powerlaw` to the `diskbb` component ($f_{\rm PL}/f_{\rm diskbb}$) gradually increased from $\lesssim$6% to ∼25%. While from $\delta t \sim 570$ days to $\delta t \sim 680$ days, this ratio appears to decrease slightly to ∼16% (Figure 6).
3. The 0.3–2 keV X-ray luminosity exhibits short-timescale dips superimposed on a long-term declining trend, which we refer to as the "envelope" of the X-ray light curve. The observed luminosity within this envelope follows $L_{\rm X} \propto (t_{\rm MJD} - 59647)^{-2.2}$, reaching a maximum of $1.5 \times 10^{44}$ erg s$^{-1}$ at $\delta t \approx 205$ days and dropping to $1.5 \times 10^{43}$ erg s$^{-1}$ at $\delta t \approx 670$ days.
4. The X-ray light curve is extremely variable on the timescale of $t_{\rm var} \sim 1$ hr–1 day during certain time intervals, such as $\delta t \sim 190$–240 days (Figure 10), and during the XMM E3 observation at $\delta t \sim 601$ days (Figure 7, right panel). However, this variability is episodic, with periods where the light curve follows a power-law decline, as

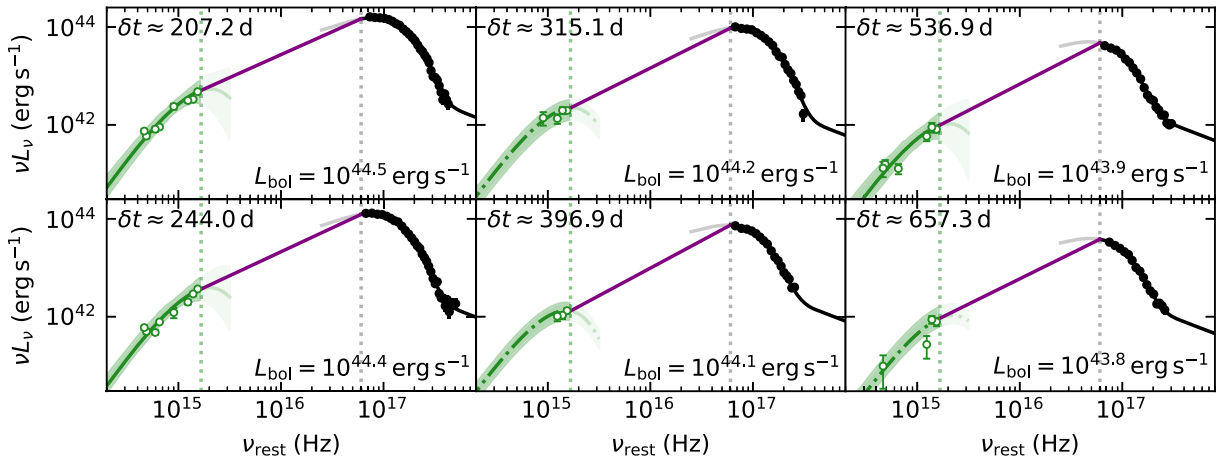


**Figure 15.** SEDs of AT2022lri at six representative epochs (marked as dashed orange line in Figure 16). The data have been corrected for extinction (in UV/optical) and Galactic absorption (in the X-ray). The green lines show blackbody fits to the UV/optical data, with solid green lines indicating epochs where the blackbody temperature is fitted and dashed–dotted green lines where the temperature is fixed (see Section 3.3). The black lines show the NICER best-fit model with Γ fixed at 2.8 (Section 4.4.2). The purple lines depict simple power-law models used as a proxy for the SED shape in the EUV band.

seen in Figure 5 and the XMM E2 light curve (Figure 7, left panel).

5. No significant periodicity was detected in the X-ray light curve.
6. In our XMM-Newton/RGS observation, no narrow emission lines are evident (Section 4.3.2). This contrasts with the only two other TDEs with high-quality RGS spectra, ASASSN-14li (J. M. Miller et al. 2015) and ASASSN-20qc (P. Kosec et al. 2023), where low-velocity ($\sim$100 km s$^{-1}$) outflows were detected.
7. In some high-SNR NICER observations, strong residuals that peak at $\sim$1 keV are clearly evident. These observations can be well described by two physically motivated models: either (1) an ionized outflow contributes additional absorption (`outflow_abs`) and emission lines (`outflow_emi`) or (2) disk reflection off an ionized slab (`reflTDE`).
8. Variations in X-ray luminosity are intrinsic to the continuum and are positively corrected with changes in the (inner) disk temperature, as seen in both basic phenomenological modeling (Section 4.4.2, Figure 11) and physically motivated modeling results (Section 4.4.4, Figure 14). The typical inner disk temperature is $\sim 10^6$ K.
9. The apparent inner disk radius $R_{\rm in}^*$ remains roughly constant at $\sim 2\times10^{11}$ cm, as determined from both basic phenomenological spectral modeling (Figure 6) and physically motivated spectral modeling (Figure 14).
10. The power-law photon index $\Gamma\sim2.8$ in basic phenomenological modeling (Section 4.2), and $\sim$3.7 in physically motivated modeling (Tables 3, 4).
11. In the first physically motivated model (absorption and emission from an ionized outflow), we obtain $N_{\rm H,\ out}\in(3.7\times10^{20},\ 3.6\times10^{21})$ cm$^{-2}$, $\log(\xi/{\rm erg\ cm\ s^{-1}})\approx3$, $v_{\rm abs}\approx-0.11c$, and $v_{\rm emi}\in(-0.16c, -0.13c)$.
12. In the second physically motivated model (disk reflection off an ionized slab), we obtain $\log(\xi/{\rm erg\ cm\ s^{-1}})\approx2.1$, $n_{\rm e}\sim10^{19}$ cm$^{-3}$, and $v_{\rm refl}\approx-0.34c$.
13. There is no evidence of neutral absorption at the host redshift.

### 5.1. Super-Eddington Accretion onto a Low-mass Massive Black Hole

#### 5.1.1. Basic Considerations: Bolometric Luminosity, Inclination, and Long-term Evolution

The BH mass of $M_{\rm BH}\approx10^5\,M_\odot$ (Section 2.3) is at the low end of ZTF-selected TDEs (Y. Yao et al. 2023). The gravitational radius is $r_{\rm g}=GM_{\rm BH}/c^2\approx1.5\times10^{10}$ cm, and the tidal radius is $R_{\rm T}\approx3\times10^{12}$ cm (for a Sun-like star). The fallback timescale is relatively short ($t_{\rm fb}\approx13$ days). The inferred $R_{\rm in}^*\approx2\times10^{11}\,{\rm cm}\sim13R_g$. As we will show later, the inclination should be very small ($\cos i\sim1$), so $R_{\rm in}$ ($\approx R_{\rm in}^*$) is close to the innermost stable circular orbit $r_{\rm ISCO}$. During the monitoring campaign, the photosphere of the UV and optical component receded from $\sim67R_{\rm T}$ to $\sim20R_{\rm T}$.

To assess the bolometric luminosity ($L_{\rm bol}$) across the X-ray "envelope" (where no strong dips are observed), we selected six epochs and integrated $\int L_\nu d\nu$ from 10000 Å to 10 keV. From 10000 Å to 1800 Å, we integrate below the blackbody model fitted to the UV/optical photometry (Section 3.3). From 0.25 to 10 keV, we integrate below the best-fit model fitted to the NICER data (Section 4.4.2). From 1800 Å to 0.25 keV, we assume that the TDE spectrum is continuous and can be approximated by a power law of $L_\nu\propto\nu^\alpha$, where $\alpha$ is determined by connecting the UV/optical blackbody at 1800 Å and the X-ray model at 0.25 keV (see Figure 15). It is interesting to notice that the purple lines have a slope that is steeper than $\nu L_\nu\propto\nu^{4/3}$ (i.e., the standard multitemperature blackbody for a constant accretion rate at all radii). A physical explanation could be that the accretion rate is not constant with radius. Since TDE fallback stream deposits mass near $R_{\rm T}$, the accretion rate at $R\gg R_{\rm T}$ must be much smaller than $\dot{M}_{\rm acc}$ at $R\leqslant R_{\rm T}$. This causes the emission from larger radii (at lower frequency) to be weaker than the prediction from the standard case.

The upper panel of Figure 16 shows the evolution of $L_{\rm bol}$, which is also compared with $L_{\rm X}$ and $L_{\rm bb}$. With $M_{\rm BH}\sim10^5\,M_\odot$, the bolometric luminosity declined from $3.2\times10^{44}$ erg s$^{-1}\approx25L_{\rm Edd}$ at $\delta t\approx207.2$ days to $6.1\times10^{43}$ erg s$^{-1}\approx5L_{\rm Edd}$ at $\delta t\approx657.3$ days. Even with the largest $M_{\rm BH}$ estimate of

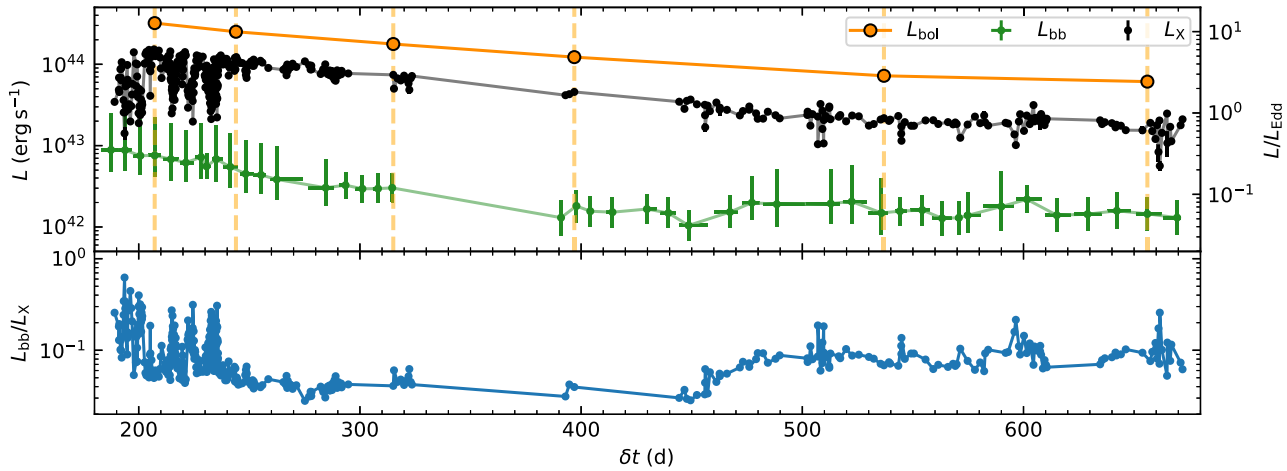


**Figure 16.** Upper: evolution of bolometric luminosity $L_{\rm bol}$, 0.3–2 keV unabsorbed X-ray luminosity $L_{\rm X}$, and blackbody luminosity of the UV/optical emission $L_{\rm bb}$. Lower: evolution of $L_{\rm bb}/L_{\rm X}$.

$\sim 10^6\,M_\odot$, $L_{\rm bol} > L_{\rm Edd}$ at $\delta t < 240$ days, suggesting that AT2022lri stayed in the super-Eddington accretion regime at least during the intense rapid X-ray dipping phase.

Recent 3D general relativistic radiation magnetohydrodynamics (GRRMHD) simulations for the TDE super-Eddington accretion flow show that copious amount of X-ray emission can only escape from the optically thin funnel along the disk axis when viewed close to face-on (L. Dai et al. 2018; B. Curd & R. Narayan 2019). L. L. Thomsen et al. (2022b) performed three simulations for mass accretion rates at 7, 24, and 24 $\dot{M}_{\rm Edd}$, showing that $L_{\rm bb}/L_{\rm X} \lesssim 0.1$ can only be produced at their smallest inclination angle ($i = 10°$).[37]

The lower panel of Figure 16 shows the ratio of $L_{\rm bb}/L_{\rm X}$. At $\delta t \lesssim 240$ days, it stays at $\lesssim$0.1 (except during the X-ray dips), pointing to a low inclination angle. From $\approx$240 days to $\approx$330 days, $L_{\rm bb}/L_{\rm X}$ exhibits a decaying trend, suggesting that the decline in UV and optical emission is faster than that in the X-ray emission. This is consistent with the expectation where, as $\dot{M}_{\rm acc}$ decreases, the optically thin funnel (along the disk axis) gets wider, and a smaller fraction of X-ray photons are being reprocessed in the optically thick outflow (L. L. Thomsen et al. 2022b). From $\approx$390 days to $\approx$672 days, $L_{\rm bb}$ stays relatively constant. Similar late-time UV and optical plateaus have been observed in many other TDEs (A. Mummery et al. 2024). It is possible that, at such late times, reprocessing becomes very weak such that the UV and optical emission is dominated by the outer edge of an accretion disk with a nearly constant outer radius of $\sim 20 R_{\rm T}$.

At the inner disk $R_{\rm in} \sim 2 \times 10^{11}$ cm, the dynamical timescale is $t_{\rm dyn} \sim \sqrt{R_{\rm in}^3/(GM_{\rm BH})} \sim 17$ s, the thermal timescale is $t_{\rm th} = \frac{1}{\alpha} t_{\rm dyn} \sim 170$ s (assuming a Shakura–Sunyaev viscosity parameter of $\alpha = 0.1$), and the viscous timescale is $t_{\rm vis} = \frac{1}{\alpha} t_{\rm dyn} (H/R)^{-2} \sim 2$ ks (assuming a disk height-to-radius ratio of $H/R = 0.3$). The orbital timescale at $R_{\rm in}$ is $\sim$110 s and at $R_{\rm T}$ is $\sim$3 hr. We see that $t_{\rm vis}$, a time in which angular momentum distribution changes due to torque caused by dissipative stresses, is comparable to the shortest observed variability timescale.

### 5.1.2. Origin of the X-Ray Dips

First, we rule out the idea that the X-ray variability is caused by changes in absorption along the line of sight, which is a leading model for a subtype of changing-look AGN termed as changing-obscuration AGN (C. Ricci & B. Trakhtenbrot 2023). As is shown in our spectral analysis, there is no evidence for elevated neutral intervening gas at the host redshift. In the `outflow_abs` spectral model, the best-fit $N_{\rm H,out}$ values are too small to account for the large amplitude of flux variations. Therefore, although the outflow might exhibit some degree of inhomogeneities/turbulence, changing obscuration itself is not the primary reason for the strong variability.

Next, we consider if the variability can be caused by global precession, which is possible when the spin of a rotating BH is misaligned with the angular momentum of the newly formed accretion disk, exerting a Lense–Thirring (LT) torque on the disk. Using a slim disk model for the disk structure (appropriate for the super-Eddington phase, L. E. Strubbe & E. Quataert 2009) and A. Franchini et al. (2016) computed the expected precession time $T_{\rm prec}$ as functions of $M_{\rm BH}$ and the dimensionless BH spin parameter $a$ (see also O. Teboul & B. D. Metzger 2023). For a $10^5\,M_\odot$ BH, $T_{\rm prec}$ reaches the minimum value of 3–4 days at the maximum $a$, which is much longer than the observed $t_{\rm var}$. Furthermore, since precession-induced light-curve modulation is expected to be periodic or quasiperiodic (N. Stone & A. Loeb 2012), we disfavor such a scenario.

If the tidal disruption resides in a massive black hole binary (MBHB), the existence of a secondary MBH would cause an observable effect to the TDE fallback rates if the debris at apocenter leaves the Roche lobe of the disrupting BH. This imposes a short binary separation at the subparsec and a binary orbital period of $T_{\rm orb} \sim 0.3$ yr (E. R. Coughlin et al. 2019). Numerical (F. K. Liu et al. 2009; A. Ricarte et al. 2016) and hydrodynamic (E. R. Coughlin et al. 2017; Q. Vigneron et al. 2018) studies suggest that light-curve dips (or interruptions) on top of a power-law decay might be expected with variability on the timescale of months to years. Since this is much longer than the $t_{\rm var}$ observed in AT2022lri, we disfavor an MBHB.

A natural reason for the observed fast X-ray dips is associated with episodic drops of mass accretion rates in the

[37] The simulations results at $i = 10°$ show even smaller values of $L_{\rm bb}/L_{\rm X} \sim 10^{-3}$ (see Figure 4 of L. L. Thomsen et al. 2022b). However, this $L_{\rm bb}$ is probably underestimated due to the fact that the post-processing radiative transfer was performed in 1D, and that the inject spectrum was a single-temperature $10^6$ K blackbody, instead of a multitemperature disk with $\sim 10^6$ K inner temperature.

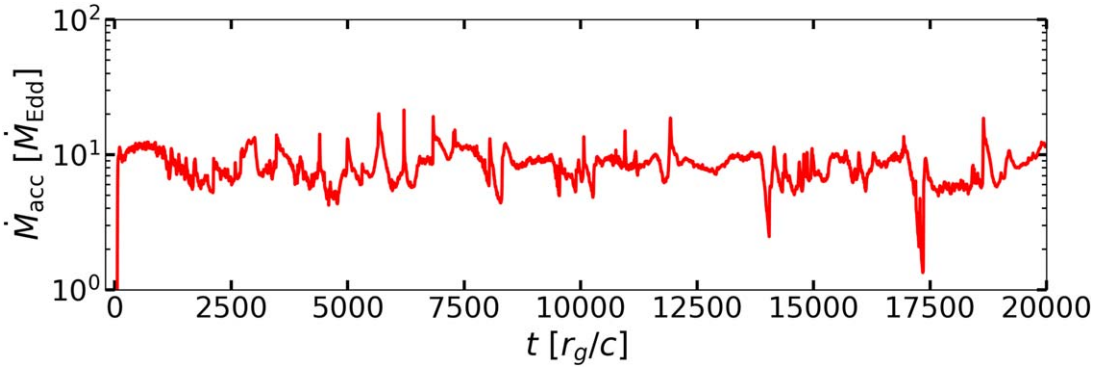


**Figure 17.** The mass accretion rate as a function of time in a simulated super-Eddington disk around a black hole with $M_{\rm BH} = 10^6 M_\odot$ and $a = 0$. The time-averaged accretion rate is around $7\dot{M}_{\rm Edd}$. The $x$-axis is in unit of gravitational time $r_g/c$.

super-Eddington accretion flow. This is hinted by the fact that $L_{\rm X} \propto T_{\rm in}^4$. The decrease in $T_{\rm in}$ reflects instantaneous changes of local heating rate and mass accretion rate at $R_{\rm in}$, which might be triggered by instabilities in the magnetic field structure. For example, in magnetically arrested disks (MADs; I. V. Igumenshchev et al. 2003; R. Narayan et al. 2003; I. V. Igumenshchev 2008), large-scale magnetic field lines threading the inner accretion flow grow to a saturation value of the (dimensionless) magnetic flux $\phi_{\rm BH}$ near the BH horizon. Then, the gas accretion process is highly governed by the interplay between magnetic flux and gas. Numerical simulations show in MADs $\phi_{\rm BH}$ exhibits substantial fluctuations around the saturated value, which therefore introduces large variability in the accretion rate $\dot{M}_{\rm acc}$ (A. Tchekhovskoy et al. 2011; J. C. McKinney et al. 2012; A. Tchekhovskoy & J. C. McKinney 2012). Recent simulations of MAD disks in the super-Eddington accretion regime demonstrate similar behaviors (A. Sadowski & R. Narayan 2016; L. Dai et al. 2018; L. L. Thomsen et al. 2022b; B. Curd & R. Narayan 2023). As a demonstration, we show the simulated $\dot{M}_{\rm acc}$ from a super-Eddington accretion disk around a $10^6 M_\odot$ BH in Figure 17. The simulation has otherwise the same setup as the lowest Eddington ratio run with $\dot{M}_{\rm acc} \sim 7\dot{M}_{\rm Edd}$ in L. L. Thomsen et al. (2022b), except that the BH spin is set to be $a = 0$. One can see that the variability over a timescale of $1000\, r_g/c \sim 1$ hr can reach from a few to $\sim$10 times, which is similar to the observed scale of variability.

Furthermore, in the simulations conducted by B. Curd & R. Narayan (2023) where $\dot{M}_{\rm acc}$ decreases from $3\dot{M}_{\rm Edd}$ to $0.3\dot{M}_{\rm Edd}$, this fluctuation in $\phi_{\rm BH}$ is directly linked to variations in $L_{\rm bol}$, irrespective of the BH spin. However, B. Curd & R. Narayan (2023) shows that quasiperiodic variability is developed in the $a = 0.9$ simulation, whereas the variability appears stochastic in the $a = 0$ simulation. This suggests that AT2022lri should be a TDE happening around a low-spin BH, which is also consistent with the fact that no evidence of on-axis relativistic jets (in the form of bright hard X-ray emission) has been observed from this system.

Another possible cause of the X-ray drops might be related to wobbling of the inner accretion disk along the MBH's spin axis. Interestingly, the host galaxy's disk component has an axis ratio close to unity ($q = 0.96$, Section 2.2), suggesting that the MBH's spin axis is probably along our line of sight. If the TDE disk's initial axis does not align with the spin axis, LT precession can naturally occur. Although we discussed previously that global precession of the entire disk only gives $t_{\rm var} \gtrsim$ few days, mass infall on shorter timescales is expected if LT torques are strong enough to tear the wrapped disk into inner and outer parts (C. Nixon et al. 2012). While this effect is shown to be most pronounced at low accretion rates, thinner disks, and larger oriented inclinations (A. Raj et al. 2021), it is still likely to happen in a thick disk if $H/R \lesssim 0.1$. In this case, the apparent drops of $T_{\rm in}$ may come from either changes in mass accretion rate or a viewing-angle effect, where at larger inclination angles the disk temperature measured in the soft X-ray band appears lower (L. Dai et al. 2018). While quasiperiodic behavior is observed in the thin disk simulation by A. Raj & C. J. Nixon (2021), one may imagine that the TDE accretion flow starts from a more asymmetric initial condition, and the inner and outer disks, instead of being discrete regions, might be weakly connected by tenuous gas, rendering a more stochastic variability. Under such a circumstance, the decrease of X-ray dipping amplitude and occurrence rate after $\delta t \sim 240$ days (see Figures 5 and 6) might signify a time when the inner disk is aligned to the BH spin, and the unstable wobbling region moves to larger radii.

#### 5.1.3. Physically Motivated Spectral Models

Two physically motivated models are explored. In the first model, we consider absorption from an ionized outflow and emission from the outflow itself. The outflow velocity from the emission component, $v_{\rm emi} \in (-0.16c,\ -0.13c)$, is slightly larger than the velocity from the absorption component ($v_{\rm abs} \approx -0.11c$). This can be realized for certain geometry where the outflow along the polar region has lower velocities than that along the equatorial region (see a schematic picture in the left panel of Figure 18).

Taking a fiducial outflow velocity of $v_{\rm out} \sim 0.15c$, we estimate the outflow launching radius to be the distance at which the observed velocity is equivalent to the escape velocity from the BH: $R_{\rm launch} = 2GM_{\rm BH}/v_{\rm out}^2 \sim 1.3 \times 10^{12}$ cm $\sim 90R_{\rm g}$. The mass outflow rate can be estimated with $\dot{M}_{\rm out} = 4\pi C_{\rm f} R_{\rm launch} N_{\rm H} \mu m_{\rm p} v_{\rm out}$ (D. R. Pasham et al. 2024a), where $C_{\rm f}$ is the covering fraction of the outflow, and $\mu = 1.4$ is the mean atomic mass per proton. Taking $C_{\rm f} = 0.5$, as the fiducial value from the literature, we have $\dot{M}_{\rm out} \sim 8.7 \times 10^{19}$ g s$^{-1}$ $\sim 1.4 \times 10^{-6}\, M_\odot$ yr$^{-1}$. The kinetic power of the outflow $\dot{E}_{\rm out} = 1/2 \dot{M}_{\rm out} v_{\rm out}^2 \sim 8.9 \times 10^{38}$ erg s$^{-1}$. Taking $\eta = 0.1$, the mass accretion rate $\dot{M}_{\rm acc} = L_{\rm bol}/(\eta c^2) \sim 3.6 \times 10^{24}$ g s$^{-1}$ $\sim 5.7 \times 10^{-2}\, M_\odot$ yr$^{-1}$. We see that the mass outflow rate is a tiny fraction ($\sim 2.4 \times 10^{-5}$) of the inflow rate. We note that the mass outflow rate estimated above should be taken as a lower limit because the launching radius could be larger than the one

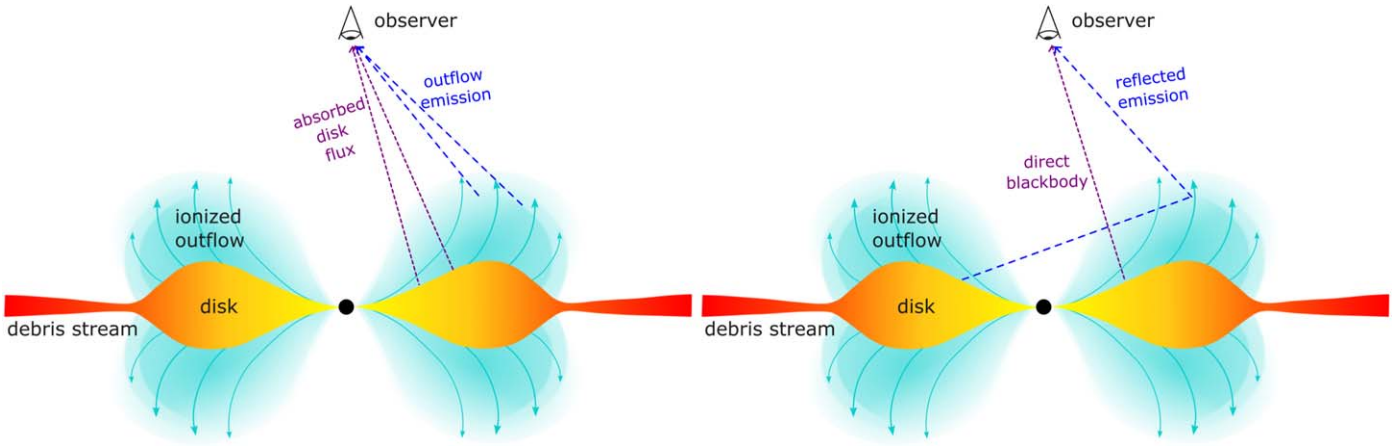


**Figure 18.** Left: A schematic picture showing the geometry of the super-Eddington accretion flow, appropriate for our modeling with an ionized outflow as the absorber. The short dashed purple lines depict line of sights where the emission is mainly absorbed disk flux, and the long dashed blue lines highlight line of sights that primarily give rise to the emission component of the outflow. Right: a schematic picture for the reflection modeling.

calculated assuming the escape velocity. Moreover, since the viewing angle is close to face-on, the column density in the absorber ($N_{\rm H}\sim 10^{21}\,{\rm cm}^{-2}$) along the line of sight will be smaller than that along other directions if the bulk of the matter ejection occurs along the equatorial plane.

In the second physically motivated model, we consider disk emission reflected off an ionized slab. A schematic of the reflection model is shown in the right panel of Figure 18. In the traditional reflection model `xillver`, the gas density is typically fixed at $n_e = 10^{15}\,{\rm cm}^{-3}$ (J. García & T. R. Kallman 2010; J. García et al. 2013). J. A. García et al. (2016) considered the change of free–free emissivity, showing that high densities lead to a hotter and more ionized atmosphere, thereby strengthening the thermal continuum at $\lesssim$2 keV. It was found that relativistic reflection off a high density disk could explain the soft X-ray excess observed in many Seyfert galaxies (J. Jiang et al. 2019). A potential issue of our modeling with `relxillTDE` (`xillverTDE`) is that the inferred gas density in model (D) is close to the maximum value of the model grid (i.e., $n\sim 10^{19}\,{\rm cm}^{-3}$). However, gas densities observed in GRRMHD simulations of super-Eddington accretion disks around TDEs are generally much lower ($n\lesssim 10^{13}\,{\rm cm}^{-3}$). Further development and extensive testing of this model may be necessary to assess how the current assumptions impact parameter constraints.

### 5.2. Comparison with Other TDEs and Nuclear Transients

Here, we compare AT2022lri with other MBH-powered transients with nonperiodic fast X-ray variability ($t_{\rm var}\lesssim$ 1 days), including jetted TDEs (Section 5.2.1), nonjetted TDEs (Section 5.2.2), as well as other nuclear transients with similar properties (Section 5.2.3).

#### 5.2.1. Jetted TDEs

First, we compare AT2022lri with TDEs associated with on-axis relativistic jets. Among the four known jetted TDEs, subhour-timescale X-ray variability has been observed in Sw J1644+57 (A. J. Levan et al. 2011; J. S. Bloom et al. 2011; D. N. Burrows et al. 2011) and AT2022cmc (D. R. Pasham et al. 2023; Y. Yao et al. 2024).

As shown in Figure 19, the X-ray light curve of AT2022lri bears some resemblance to that of Sw J1644+57 in that both objects exhibit peak X-ray luminosities above the Eddington limit, and X-ray dips with $t_{\rm var}<1$ hr on top of power-law light-curve declines. A blueshifted emission line (E. Kara et al. 2016) and hints of periodicity have been reported in Sw J1644 +57 (C. J. Saxton et al. 2012; W.-H. Lei et al. 2013; R.-F. Shen & C. D. Matzner 2014; A. Franchini et al. 2016). C. J. Saxton et al. (2012) reported quasiperiodicity at multiple periods, which is thought to come from modulation of the jet luminosity by the disk precession and nutation. W.-H. Lei et al. (2013) argues that there exists a $T=2.7$ day quasiperiodicity that lasts about 10 days, which might be related to MAD around rapidly spinning massive BHs (A. Tchekhovskoy et al. 2014) or instabilities at the nozzle point when the tidally disrupted star returns to pericenter (F. De Colle et al. 2012). As noted by B. Curd & R. Narayan (2023), it is possible that flux eruption events in MAD drive the X-ray variability after $\sim$10 days (when a spin-aligned jet is established).

We note that, despite the similarities between the X-ray light curves of AT2022lri to that of Sw J1644+57, the emission mechanisms are different. Jetted TDEs generally exhibit much harder X-ray spectra that can be modeled with synchrotron or inverse Compton processes, probably powered by internal energy dissipation with the jet (D. N. Burrows et al. 2011; Y. Yao et al. 2024). The lack of hard X-ray emission in AT2022lri suggests the absence of a collimated relativistic jet.

#### 5.2.2. Nonjetted TDEs

X-ray variability of TDEs is a subject of vigorous investigation.

Large-amplitude (i.e., flux variation with a multiplicative factor $\gtrsim$5) X-ray variability on the timescale of a few days has been previously observed in the TDE SDSS J1201+30 (R. D. Saxton et al. 2012), 2MASX 0740−85 (R. D. Saxton et al. 2017), OGLE16aaa (J. J. E. Kajava et al. 2020), AT2019azh (J. T. Hinkle et al. 2021), AT2019ehz (S. van Velzen et al. 2021; M. Guolo et al. 2024), AT2020ocn (D. R. Pasham et al. 2024b), and the TDE candidates AT2019avd (Y. Wang et al. 2023). They have been interpreted as TDEs in MBHBs (F. K. Liu et al. 2014; X. Shu et al. 2020), LT precession, brief glimpses through a patchy reprocessing layer with "gaps," and clumpy outflows at $\sim 500R_{\rm g}$ from the BH in supercritical accretion (S. Takeuchi et al. 2013; H. Kobayashi et al. 2018). However, as elaborated in

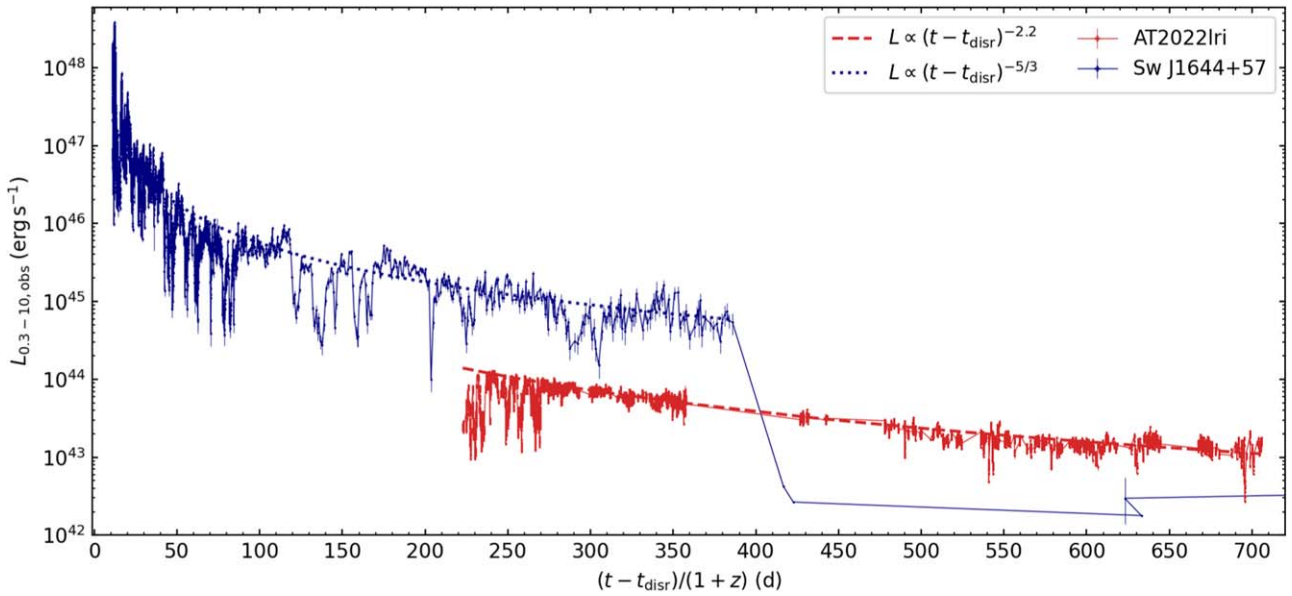


**Figure 19.** Isotropic equivalent X-ray luminosity of AT2022lri and Sw J1644+57 (A. J. Levan et al. 2016; V. Mangano et al. 2016; T. Eftekhari et al. 2018) in the observer frame 0.3–10 keV, plotted as a function of rest-frame days since the assumed disruption epoch $t_{disr}$. For AT2022lri, we adopt $t_{disr} = 59647$ (in MJD; see Section 4.4.2); for Sw J1644+57, we adopt $t_{disr} = t_{trig} - 15$ days (A. Tchekhovskoy et al. 2014), where $t_{trig}$ is MJD 55648.5401.

Section 5.1.2, these explanations encounter challenges in accounting for the variability timescales and X-ray spectra observed in AT2022lri.

Moderate amplitude (i.e., flux variation with a multiplicative factor $\gtrsim$2) variability on an hour timescale is seen in the TDE candidate eRASSt J234402.9−352640 (D. Homan et al. 2023). However, the lower cadence in the X-ray light curve of eRASSt J234402.9−352640 prohibits identification of dips atop a power-law decline, and it is not clear if the absence of spectral features is a result of the low SNR. We do note that the BH mass of eRASSt J234402.9−352640 is much greater ($M_{BH} \sim 10^8\,M_\odot$), indicating $\lambda_{Edd} < 0.1$ and perhaps a geometrically thinner disk.

Why do we see hour-timescale intermittent soft X-ray variability in AT2022lri, but not other TDEs? One plausible explanation involves a low-mass BH ($M_{BH} \lesssim 10^6\,M_\odot$). In this scenario, the viscous timescale $t_{vis} \lesssim 1$ hr, allowing fluctuations in $\dot{M}_{acc}$ on timescales longer than $t_{vis}$ to be promptly reflected in the observed X-ray luminosity and disk temperature. Additionally, a lower-mass BH results in a hotter inner disk, causing the emission to peak in the soft X-ray band. Moreover, the mass fallback rate can remain above the Eddington limit for an extended period, facilitating the development of a super-Eddington MAD and the associated magnetic instability.

Another possible factor is the geometry of the system. If the fast variability is driven by magnetic instability in MADs, a small inclination along the optically thin region is required. X-ray photons have more difficulty escaping along larger inclinations with higher densities, due to photon trapping and reprocessing into the UV/optical band (L. Dai et al. 2018). Short-timescale X-ray variability can also be smeared out at larger inclination angles, as the radiation is expected to interact with the disk up to large radii (A. Sadowski & R. Narayan 2016). Alternatively, if the variability is caused by a disk wobbling, a small angle between the galaxy disk axis and the observer's line of sight is needed. We note that this condition is satisfied in AT2022lri (Section 2.2).

From an observational standpoint, only a limited number of TDEs have been subjected to high-cadence X-ray monitoring. AT2022lri stands out as the only TDE with observed nonperiodic hour-timescale soft X-ray variability. However, the scarcity of comparable data, and to some degree the lack of a systematic X-ray analysis focused on short-timescale variability for other TDEs, makes it challenging to determine whether this variability is truly very rare or simply undetected in some other cases. To quantify the occurrence rate of such fast X-ray variability in future TDEs, high-cadence X-ray monitoring of nearby, X-ray-bright TDEs is essential.[38] Expanding this observational sample will be crucial for understanding the conditions under which such variability occurs and how AT2022lri compares to the broader TDE population.

### 5.2.3. Other Nuclear Transients

Using similar X-ray spectral analysis techniques as adopted in our modeling with an ionized absorber, subrelativistic outflows have been detected in a few AGN that exhibit X-ray dips on the timescale of $\sim$ months, such as the radio-loud AGN 3C 111 (F. Tombesi et al. 2012) and the radio-quiet AGN PG 1448+273 (M. Laurenti et al. 2021). The former has a BH mass of $M_{BH} \sim 2 \times 10^8\,M_\odot$ (R. Chatterjee et al. 2011), whereas the latter has $M_{BH} \sim 2 \times 10^7\,M_\odot$. The outflows in these AGNs are of much higher column densities $N_H \sim 10^{23}\,cm^{-2}$ and ionization ($\log\,\xi \sim 5$). It has been proposed that these X-ray dips could be directly linked to a depletion of the inner accretion disk caused by the material being expelled through the outflow (F. Tombesi et al. 2012; M. Laurenti et al. 2021)—a picture that is different from what we propose in Section 5.1.2.

The 1 keV residual feature seen in AT2022lri looks reminiscent to the 2018–2019 X-ray observations of 1ES 1927+654. This object was a well-known type 2 AGN (see

[38] An relatively high X-ray flux level ($\gtrsim 10^{-12}$ erg s$^{-1}$ cm$^{-2}$) is needed to obtain sufficient statistics to reveal order-of-magnitude flux changes.

L. C. Gallo et al. 2013 and references therein). On 2017 December 23, the ASASSN survey detected an optical flare, the light-curve evolution of which follows the canonical slow rise and power-law decay normally observed in TDEs (B. Trakhtenbrot et al. 2019). Extensive follow-up X-ray observations starting from 2018 May revealed that the preexisting AGN corona (signified by the power-law component) was first destroyed in the event and was recreated around 1 yr after the optical discovery (C. Ricci et al. 2020). The host BH has $M_{\rm BH} \sim 10^6\,M_\odot$ (R. Li et al. 2022). C. Ricci et al. (2021) presented the short-timescale ($t_{\rm var} < 5$–$10$ ks) large-amplitude X-ray variability, studied the spectral evolution, and modeled the 1 keV spectral feature using both symmertric Gaussian lines and relativistically broadened asymmetric line profiles (i.e., the `relline` model, T. Dauser et al. 2010, 2013). It was found that the X-ray luminosity increases with the disk temperature, with an average power-law slope of $b \approx 3.85$ (a relation similar to what we see in AT2022lri; see Figure 11), although the trend is steeper (flatter) at lower (higher) luminosities in 1ES 1927+654. M. Masterson et al. (2022) applied `xillverTDE` and successfully explained the spectral shape using blurred reflection, with best-fit spectral parameters similar to what we found in model (D). 1ES 1927+654, as a special changing-state AGN with no prior analogs, has been interpreted as a TDE in a preexisting AGN (B. Trakhtenbrot et al. 2019; C. Ricci et al. 2020) and a "magnetic flux inversion" event (S. Laha et al. 2022). Given the similarities between AT2022lri and 1ES 1927+654, it might be the same physical mechanism that drives the fast variability in both systems.

## 6. Summary and Conclusions

We have presented an extensive multiwavelength study of the TDE AT2022lri. The main results from our work are as follows:

1. At a redshift of $z = 0.03275$, the host of AT2022lri is a quiescent galaxy that can be modeled with a disk component viewed face-on and a pseudo bulge component. It has a total stellar mass of $\sim 10^{9.6}\,M_\odot$, a BH mass of $\sim 10^5\,M_\odot$, and no historical X-ray detection at $\lesssim 2.5 \times 10^{41}$ erg s$^{-1}$ (Section 2).
2. AT2022lri belongs to the TDE-H+He optical spectroscopic subtype (Section 3.4).
3. The X-ray light curve from $\delta t \sim 190$ days to $\sim 680$ days exhibits dips atop a power law that declines from $1.5 \times 10^{44}$ erg s$^{-1}$ to $1.5 \times 10^{43}$ erg s$^{-1}$. The dips have amplitudes on the order of $\approx$2–8 and timescales of $\approx$0.5 hr–1 day. Fast X-ray variability shows up at intermittent phases and persists throughout our monitoring program (see Figure 5).
4. The bolometric luminosity remains above the Eddington limit at $\delta t \lesssim 240$ days (and perhaps beyond; see Figure 16). The ratio between the UV and optical blackbody luminosity to that of the X-ray luminosity remains small ($L_{\rm bb}/L_{\rm X} \lesssim 0.1$), suggesting a super-Eddington accretion flow viewed face-on. This interpretation is fairly insensitive to the inferred BH mass within a reasonable range of $10^4$–$10^6\,M_\odot$.
5. When fitted with simple continuum models, the X-ray spectra of AT2022lri exhibit a strong residual that peaks around 1 keV. The spectral features can be well modeled with either absorption and emission from a blueshifted ($v_{\rm out} \sim 0.1c$) ionized absorber ($N_{\rm H} \sim 10^{21}$ cm$^{-2}$, log $\xi \sim 3$) or reflection off a dense outflow ($v_{\rm out} \sim 0.3c$). These two models are statistically comparable and physically feasible. Both models suggest the existence of subrelativistic outflows that are consistent with various simulations of disk winds from super-Eddington accretion disks.
6. There is no clear evidence of narrow absorption lines similar to those observed in ASASSN-14li (J. M. Miller et al. 2015) and ASASSN-20qc (P. Kosec et al. 2023) in the RGS spectrum (Section 4.3.2).
7. The intermittent strong X-ray dips correspond to drops of the inner disk temperature. We propose that this is a result of episodic drops of mass accretion rates at the inner disk triggered by magnetic instability or/and wobbling of the inner disk along the BH's spin axis (Section 5.1.2).

In the future, continued observations of AT2022lri are important to further track the evolution of the accretion flow and reveal possible state transitions. An in-depth X-ray timing analysis is needed to search for quasiperiodic oscillations and reverberation signals, and to reveal connections to other accreting BH systems. Radio observations of AT2022lri will be particularly useful to probe the galaxy circumnuclear matter density profile and the outflow velocity evolution (K. D. Alexander et al. 2020), which might serve as a diagnostic for the two spectral models.

Looking ahead, a systematic timing analysis on all TDEs with high-cadence observations is needed to address the ubiquity and physical origins of short-timescale X-ray variability in TDEs. Next-generation X-ray instruments such as the Advanced X-ray Imaging Satellite will be able to extend the energy coverage and potentially directly differentiate the spectral models (C. S. Reynolds et al. 2023; R. Arcodia et al. 2024).

## Acknowledgments

We thank Norbert Schartel for approving our XMM-Newton ToO requests. We thank Andrew Mummery, Chris Nixon, Nick Stone, Anil Seth, Luis C. Ho, Hua Feng, Peter Kosec, and Junjie Mao for helpful discussions.

Y.Y. and S.R.K. acknowledge support from NASA under award Nos. 80NSSC22K1347 and 80NSSC24K0534. M.G. and S.G. are supported in part by NASA XMM-Newton grants 80NSS23K06215 and 80NSSC22K0571. F.T. acknowledges funding from the European Union—Next Generation EU, PRIN/MUR 2022 (2022K9N5B4). R.L. was supported by the National Science Foundation of China (11721303, 11991052, 12011540375, 12233001), the National Key R&D Program of China (2022YFF0503401), and the China Manned Space Project (CMS-CSST-2021-A04, CMS-CSST-2021-A06). L.D. and T.K. acknowledge support from the National Natural Science Foundation of China and the Hong Kong Research Grants Council (12122309, 17305920, 17314822, 27305119). This research was supported in part by grant No. NSF PHY-2309135 to the Kavli Institute for Theoretical Physics (KITP).

This work is based on observations obtained with the Samuel Oschin Telescope 48 inch and the 60 inch Telescope at the Palomar Observatory as part of the Zwicky Transient Facility project. ZTF is supported by the National Science Foundation under grant No. AST-2034437 and a collaboration including

Caltech, IPAC, the Weizmann Institute of Science, the Oskar Klein Center at Stockholm University, the University of Maryland, Deutsches Elektronen-Synchrotron and Humboldt University, the TANGO Consortium of Taiwan, the University of Wisconsin at Milwaukee, Trinity College Dublin, Lawrence Livermore National Laboratories, IN2P3, University of Warwick, Ruhr University Bochum, Cornell University, and Northwestern University. Operations are conducted by COO, IPAC, and UW.

SED Machine is based upon work supported by the National Science Foundation under grant No. 1106171.

The ZTF forced-photometry service was funded under the Heising-Simons Foundation grant No. 12540303 (PI: Graham).

This work has made use of data from the Asteroid Terrestrial-impact Last Alert System (ATLAS) project. The Asteroid Terrestrial-impact Last Alert System (ATLAS) project is primarily funded to search for near-Earth asteroids through NASA grants NN12AR55G, 80NSSC18K0284, and 80NSSC18K1575; byproducts of the NEO search include images and catalogs from the survey area. This work was partially funded by Kepler/K2 grant J1944/80NSSC19K0112 and HST GO-15889, and STFC grants ST/T000198/1 and ST/S006109/1. The ATLAS science products have been made possible through the contributions of the University of Hawaii Institute for Astronomy, the Queen's University Belfast, the Space Telescope Science Institute, the South African Astronomical Observatory, and The Millennium Institute of Astrophysics (MAS), Chile.

Some of the data presented herein were obtained at Keck Observatory, which is a private 501(c)3 non-profit organization operated as a scientific partnership among the California Institute of Technology, the University of California, and the National Aeronautics and Space Administration. The Observatory was made possible by the generous financial support of the W. M. Keck Foundation. The authors wish to recognize and acknowledge the very significant cultural role and reverence that the summit of Maunakea has always had within the Native Hawaiian community. We are most fortunate to have the opportunity to conduct observations from this mountain.

A major upgrade of the Kast spectrograph on the Shane 3 m telescope at Lick Observatory, led by Brad Holden, was made possible through generous gifts from the Heising-Simons Foundation, William and Marina Kast, and the University of California Observatories. Research at Lick Observatory is partially supported by a generous gift from Google.

*Software*: `astropy` (Astropy Collaboration et al. 2013), `emcee` (D. Foreman-Mackey et al. 2013), GALFITS (R. Li & L. C. Ho 2024, in preparation), `heasoft` (NASA High Energy Astrophysics Science Archive Research Center (Heasarc) 2014), `LPipe` (D. A. Perley 2019), `matplotlib` (J. D. Hunter 2007), `SAS` (C. Gabriel et al. 2004), `scipy` (P. Virtanen et al. 2020), `xspec` (K. A. Arnaud 1996).

## Appendix A
## Photometry and Observing Logs

The UV and optical photometry of AT2022lri is given in Table 5. Note that the UVOT photometry is host subtracted. The host galaxy UV AB magnitudes (corrected for Galactic extinction) from our SED model are $uvw2_{\rm UVOT} = 22.30 \pm 0.05$, $uvm2_{\rm UVOT} = 22.09 \pm 0.05$, $uvw1_{\rm UVOT} = 20.78 \pm 0.05$, and $U_{\rm UVOT} = 19.03 \pm 0.05$.

A log of low-resolution optical spectroscopic observation is given in Table 6.

A log of XMM-Newton observations is given in Table 7.

**Table 5**
UV and Optical Photometry of AT2022lri

| MJD | Instrument | Filter | $f_\nu$ ( $\mu$Jy) | $\sigma_{f_\nu}$ ( $\mu$Jy) |
|---|---|---|---|---|
| 59874.9048 | ATLAS | *o* | 64.42 | 4.34 |
| 59875.6055 | UVOT | *uvm2* | 119.69 | 7.77 |
| 59875.6080 | UVOT | *uvw1* | 108.98 | 8.34 |
| 59875.6094 | UVOT | *U* | 99.99 | 13.40 |
| 59875.6128 | UVOT | *uvw2* | 161.98 | 7.77 |
| 59877.0948 | ATLAS | *c* | 72.29 | 2.94 |
| 59880.3359 | ZTF | *r* | 75.75 | 7.84 |
| 59880.3567 | ZTF | *g* | 68.67 | 5.48 |

**Note.** $f_\nu$ is flux density corrected for Galactic extinction.

(This table is available in its entirety in machine-readable form in the online article.)

**Table 6**
Log of AT2022lri Low-resolution Optical Spectroscopy

| Start Date | $\delta t$ (days) | Telescope | Instrument | Wavelength Range (Å) | Slit Width (arcsec) | Exp. (s) |
|---|---|---|---|---|---|---|
| 2022-09-05.3 | 140.7 | P60 | SEDM | 3770–9223 | ⋯ | 2250 |
| 2022-09-15.3 | 150.4 | P60 | SEDM | 3770–9223 | ⋯ | 2250 |
| 2022-09-26.3 | 161.0 | P60 | SEDM | 3770–9223 | ⋯ | 2250 |
| 2022-10-11.4 | 175.6 | P200 | DBSP | 3200–5550, 5750–9995 | 1.0 | 1800 |
| 2022-10-26.4 | 190.2 | P200 | DSBP | 3200–5550, 5750–9995 | 1.5 | 1200 |
| 2022-10-31.3 | 194.9 | LDT | De Veny | 3586–8034 | 1.5 | 2800 |
| 2022-11-16.3 | 210.4 | Lick 3 m | Kast | 3525–10500 | 2.0 | 3660/3600[a] |
| 2022-11-17.4 | 211.5 | Keck I | LRIS | 3200–10250 | 1.5 | 600 |
| 2022-11-18.2 | 212.3 | P200 | DBSP | 3200–5550, 5750–9995 | 1.5 | 1500 |
| 2022-11-30.3 | 224.0 | Lick 3 m | Kast | 3525–10,500 | 2.0 | 3660/3600[a] |
| 2023-01-16.3 | 269.5 | Keck I | LRIS | 3200–10,250 | 1.0 | 600 |
| 2023-08-25.5 | 483.7 | Lick 3 m | Kast | 3525–10,500 | 2.0 | 3660/3600[a] |
| 2023-10-17.5 | 535.0 | Keck I | LRIS | 3200–10,250 | 1.0 | 900 |

**Notes.** All spectra will be made available on the TNS page of this source (https://www.wis-tns.org/object/2022lri) at the time of manuscript acceptance.
[a] Exposure times on blue/red sides of the spectrograph.

**Table 7**
XMM-Newton Observation Log

| Index | obsID | Exp. (ks) | Start Date (UT) | $\delta t$ (days) |
|---|---|---|---|---|
| XMM E1 | 0882591901[a] | 23.0 | 2022 Dec 26 | 249.2 |
| XMM E2 | 0915390201[b] | 75.5 | 2023 Jan 5 | 259.7 |
| XMM E3 | 0932390701[c] | 43.0 | 2023 Dec 24 | 601.0 |

**Notes.**
[a] GO program, PI: S. Gezari.
[b] DDT request submitted by M. Guolo.
[c] DDT request submitted by Y. Yao.

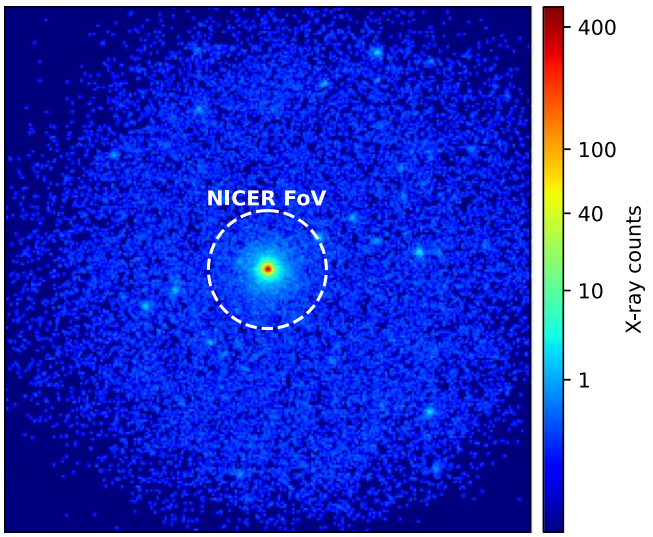


**Figure 20.** Stacked XRT (0.3–10 keV) image centered around AT2022lri. The NICER FoV is shown by the dashed circle with a radius of 3′.1.

## Appendix B
## Details of X-Ray Analysis

### *B.1. X-Ray Environment*

We created a stacked XRT image of AT2022lri using all available XRT observations. Figure 20 shows that AT2022lri is the only bright X-ray object within the NICER FoV.

### *B.2. Sanity Checks of Physically Motivated Models*

We performed a few sanity checks to validate the physically motivated models adopted in Section 4.4.4.

First, in model (C), to explore the possibility of a lower turbulent velocity, we created `XSTAR` model grids (`outflow_abs` and `emi`) with $v_{\rm turb} = 10^3\,{\rm km\,s^{-1}}$ and conducted the same modeling processes. We found that the original model grids with $v_{\rm turb} = 10^4\,{\rm km\,s^{-1}}$ provide statistically better fits.

Next, the ionization parameter $\xi \equiv L/(nR^2)$, where $L$ is the luminosity of the incident radiation, $n$ is the gas density, and $R$ is the distance from the radiation source (T. Kallman & M. Bautista 2001). Therefore, under the condition where $n$ and $R$ do not change during the rapid X-ray variability, one might expect the ionization parameter to be correlated with the incident luminosity. To investigate this scenario in the absorption/emission modeling, we compute the 1–1000 Ryd `diskbb` X-ray luminosity in the best-fit model (C), corrected for both Galactic absorption and absorption from the ionized absorber. We refit the model to the seven observations by fixing the log$\xi$ parameter based on log $L$, with the log$\xi$ value in sp6 set at 3.00. The new best-fit model yields $\chi^2/{\rm dof} = 109.63/98$, with best-fit spectral parameters closely matching those in Table 3. Specifically, the outflow exhibits $v_{\rm abs}/c = -0.124$, $v_{\rm emi}/c = -0.155$, and $N_{\rm H,\ out} \in [0.59, 9.88] \times 10^{21}\,{\rm cm^{-2}}$. Similarly, for the reflection modeling, we compute the 1–1000 Ryd `bbody` X-ray luminosity in the best-fit model (D), corrected for Galactic absorption. We refit the model to the seven observations, and fixed the log$\xi$ parameter based on log$L$, with the log$\xi$ value in sp2 fixed at 2.14. The new best-fit model gives $\chi^2/{\rm dof} = 112.80/105$, with best-fit spectral parameters very similar to what is shown in Table 4. Specifically, the outflow exhibits $\log(n/{\rm cm^{-3}}) = 18.19$ and $v_{\rm refl}/c = -0.342$. We conclude that our spectral modeling results do not sensitively depend on small variations in the log$\xi$ parameter.

Finally, since the system is inferred to be close to face-on (Section 5.1.1), we refit the seven observations by imposing $i = 18\overset{\circ}{.}20$ (instead of $i = 45°$) in model (D), where $18\overset{\circ}{.}20$ is the smallest $i$ value in the model grid of `xillverTDE`. The best-

fit model has $\chi^2/\mathrm{dof} = 111.61/104$, with best-fit parameters closely matching those shown in Table 4. This verifies that the reflection modeling result is not sensitive to the assumed inclination parameter.

## ORCID iDs

Yuhan Yao https://orcid.org/0000-0001-6747-8509
Muryel Guolo https://orcid.org/0000-0002-5063-0751
Francesco Tombesi https://orcid.org/0000-0002-6562-8654
Ruancun Li https://orcid.org/0000-0001-8496-4162
Suvi Gezari https://orcid.org/0000-0003-3703-5154
Javier A. García https://orcid.org/0000-0003-3828-2448
Lixin Dai https://orcid.org/0000-0002-9589-5235
Ryan Chornock https://orcid.org/0000-0002-7706-5668
Wenbin Lu https://orcid.org/0000-0002-1568-7461
S. R. Kulkarni https://orcid.org/0000-0001-5390-8563
Keith C. Gendreau https://orcid.org/0000-0001-7115-2819
Dheeraj R. Pasham https://orcid.org/0000-0003-1386-7861
S. Bradley Cenko https://orcid.org/0000-0003-1673-970X
Erin Kara https://orcid.org/0000-0003-0172-0854
Raffaella Margutti https://orcid.org/0000-0003-4768-7586
Yukta Ajay https://orcid.org/0009-0007-8764-9062
Thomas Wevers https://orcid.org/0000-0002-4043-9400
Tom M. Kwan https://orcid.org/0000-0003-0509-2541
Igor Andreoni https://orcid.org/0000-0002-8977-1498
Joshua S. Bloom https://orcid.org/0000-0002-7777-216X
Andrew J. Drake https://orcid.org/0000-0003-0228-6594
Matthew J. Graham https://orcid.org/0000-0002-3168-0139
Erica Hammerstein https://orcid.org/0000-0002-5698-8703
Russ R. Laher https://orcid.org/0000-0003-2451-5482
Natalie LeBaron https://orcid.org/0000-0002-2249-0595
Ashish A. Mahabal https://orcid.org/0000-0003-2242-0244
Brendan O'Connor https://orcid.org/0000-0002-9700-0036
Josiah Purdum https://orcid.org/0000-0003-1227-3738
Vikram Ravi https://orcid.org/0000-0002-7252-5485
Huei Sears https://orcid.org/0000-0001-8023-4912
Yashvi Sharma https://orcid.org/0000-0003-4531-1745
Roger Smith https://orcid.org/0000-0001-7062-9726
Jesper Sollerman https://orcid.org/0000-0003-1546-6615
Jean J. Somalwar https://orcid.org/0000-0001-8426-5732
Avery Wold https://orcid.org/0000-0002-9998-6732

## References

Abramowicz, M. A., Czerny, B., Lasota, J. P., & Szuszkiewicz, E. 1988, ApJ, 332, 646
Ajay, Y., Pasham, D. R., Wevers, T., et al. 2024, arXiv:2401.12908
Alexander, K. D., van Velzen, S., Horesh, A., & Zauderer, B. A. 2020, SSRv, 216, 81
Andalman, Z. L., Liska, M. T. P., Tchekhovskoy, A., Coughlin, E. R., & Stone, N. 2022, MNRAS, 510, 1627
Angus, C. R., Baldassare, V. F., Mockler, B., et al. 2022, NatAs, 6, 1452
Arcodia, R., Bauer, F. E., Cenko, S. B., et al. 2024, Univ, 10, 316
Arnaud, K. A. 1996, in ASP Conf. Ser. 101, Astronomical Data Analysis Software and Systems V, ed. G. H. Jacoby & J. Barnes (San Francisco, CA: ASP), 17
Astropy Collaboration, Robitaille, T. P., Tollerud, E. J., et al. 2013, A&A, 558, A33
Bellm, E. C., Kulkarni, S. R., Graham, M. J., et al. 2019, PASP, 131, 018002
Blagorodnova, N., Neill, J. D., Walters, R., et al. 2018, PASP, 130, 035003
Bloom, J. S., Giannios, D., Metzger, B. D., et al. 2011, Sci, 333, 203
Bonnerot, C., & Lu, W. 2020, MNRAS, 495, 1374
Bonnerot, C., Rossi, E. M., Lodato, G., & Price, D. J. 2016, MNRAS, 455, 2253
Burrows, D. N., Hill, J. E., Nousek, J. A., et al. 2005, SSRv, 120, 165
Burrows, D. N., Kennea, J. A., Ghisellini, G., et al. 2011, Natur, 476, 421
Cappellari, M. 2017, MNRAS, 466, 798
Cappellari, M., & Emsellem, E. 2004, PASP, 116, 138
Cardelli, J. A., Clayton, G. C., & Mathis, J. S. 1989, ApJ, 345, 245
Cenko, S. B., Fox, D. B., Moon, D.-S., et al. 2006, PASP, 118, 1396
Chambers, K. C., Magnier, E. A., Metcalfe, N., et al. 2016, arXiv:1612.05560
Charalampopoulos, P., Leloudas, G., Malesani, D. B., et al. 2022, A&A, 659, A34
Chartas, G., Cappi, M., Vignali, C., et al. 2021, ApJ, 920, 24
Chatterjee, R., Marscher, A. P., Jorstad, S. G., et al. 2011, ApJ, 734, 43
Coughlin, E. R., Armitage, P. J., Lodato, G., & Nixon, C. J. 2019, SSRv, 215, 45
Coughlin, E. R., Armitage, P. J., Nixon, C., & Begelman, M. C. 2017, MNRAS, 465, 3840
Coughlin, M. W., Bloom, J. S., Nir, G., et al. 2023, ApJS, 267, 31
Curd, B., & Narayan, R. 2019, MNRAS, 483, 565
Curd, B., & Narayan, R. 2023, MNRAS, 518, 3441
Dai, J. L., Lodato, G., & Cheng, R. 2021, SSRv, 217, 12
Dai, L., McKinney, J. C., Roth, N., Ramirez-Ruiz, E., & Miller, M. C. 2018, ApJL, 859, L20
Dauser, T., Garcia, J., Wilms, J., et al. 2013, MNRAS, 430, 1694
Dauser, T., Wilms, J., Reynolds, C. S., & Brenneman, L. W. 2010, MNRAS, 409, 1534
De Colle, F., Guillochon, J., Naiman, J., & Ramirez-Ruiz, E. 2012, ApJ, 760, 103
Dekany, R., Smith, R. M., Riddle, R., et al. 2020, PASP, 132, 038001
den Herder, J. W., Brinkman, A. C., Kahn, S. M., et al. 2001, A&A, 365, L7
Dey, A., Schlegel, D. J., Lang, D., et al. 2019, AJ, 157, 168
Eftekhari, T., Berger, E., Zauderer, B. A., Margutti, R., & Alexander, K. D. 2018, ApJ, 854, 86
Evans, C. R., & Kochanek, C. S. 1989, ApJL, 346, L13
Evans, P. A., Beardmore, A. P., Page, K. L., et al. 2007, A&A, 469, 379
Evans, P. A., Beardmore, A. P., Page, K. L., et al. 2009, MNRAS, 397, 1177
Fan, X., Bañados, E., & Simcoe, R. A. 2023, ARA&A, 61, 373
Ferrarese, L., & Ford, H. 2005, SSRv, 116, 523
Fisher, D. B., & Drory, N. 2008, AJ, 136, 773
Foreman-Mackey, D., Hogg, D. W., Lang, D., & Goodman, J. 2013, PASP, 125, 306
Franchini, A., Lodato, G., & Facchini, S. 2016, MNRAS, 455, 1946
Fremling, C., Miller, A. A., Sharma, Y., et al. 2020, ApJ, 895, 32
French, K. D., Wevers, T., Law-Smith, J., Graur, O., & Zabludoff, A. I. 2020, SSRv, 216, 32
Gabriel, C., Denby, M., Fyfe, D. J., et al. 2004, in ASP Conf. Ser. 314, Astronomical Data Analysis Software and Systems (ADASS) XIII, ed. F. Ochsenbein, M. G. Allen, & D. Egret (San Francisco, CA: ASP), 759
Gaia Collaboration, Vallenari, A., Brown, A. G. A., et al. 2023, A&A, 674, A1
Gallo, L. C., MacMackin, C., Vasudevan, R., et al. 2013, MNRAS, 433, 421
Gao, H., Ho, L. C., Barth, A. J., & Li, Z.-Y. 2020, ApJS, 247, 20
García, J., Dauser, T., Reynolds, C. S., et al. 2013, ApJ, 768, 146
García, J., & Kallman, T. R. 2010, ApJ, 718, 695
García, J. A., Fabian, A. C., Kallman, T. R., et al. 2016, MNRAS, 462, 751
Gendreau, K. C., Arzoumanian, Z., Adkins, P. W., et al. 2016, Proc. SPIE, 9905, 99051H
Gezari, S. 2021, ARA&A, 59, 21
Graham, M. J., Kulkarni, S. R., Bellm, E. C., et al. 2019, PASP, 131, 078001
Greene, J. E., Strader, J., & Ho, L. C. 2020, ARA&A, 58, 257
Guolo, M., Gezari, S., Yao, Y., et al. 2024, ApJ, 966, 160
Hammerstein, E., van Velzen, S., Gezari, S., et al. 2023, ApJ, 942, 9
Hayasaki, K., Stone, N., & Loeb, A. 2016, MNRAS, 461, 3760
HI4PI Collaboration, Ben Bekhti, N., Flöer, L., et al. 2016, A&A, 594, A116
Hinkle, J. T., Holoien, T. W.-S., Auchettl, K., et al. 2021, MNRAS, 500, 1673
Holoien, T. W.-S., Prieto, J. L., Bersier, D., et al. 2014, MNRAS, 445, 3263
Homan, D., Krumpe, M., Markowitz, A., et al. 2023, A&A, 672, A167
Hunter, J. D. 2007, CSE, 9, 90
Igumenshchev, I. V. 2008, ApJ, 677, 317
Igumenshchev, I. V., Narayan, R., & Abramowicz, M. A. 2003, ApJ, 592, 1042
Jiang, J., Fabian, A. C., Dauser, T., et al. 2019, MNRAS, 489, 3436
Jiang, Y.-F., Guillochon, J., & Loeb, A. 2016, ApJ, 830, 125
Kaastra, J. S., & Bleeker, J. A. M. 2016, A&A, 587, A151
Kajava, J. J. E., Giustini, M., Saxton, R. D., & Miniutti, G. 2020, A&A, 639, A100
Kallman, T., & Bautista, M. 2001, ApJS, 133, 221
Kara, E., Dai, L., Reynolds, C. S., & Kallman, T. 2018, MNRAS, 474, 3593
Kara, E., Miller, J. M., Reynolds, C., & Dai, L. 2016, Natur, 535, 388
Kim, Y. L., Rigault, M., Neill, J. D., et al. 2022, PASP, 134, 024505
Kobayashi, H., Ohsuga, K., Takahashi, H. R., et al. 2018, PASJ, 70, 22
Kormendy, J., & Ho, L. C. 2013, ARA&A, 51, 511

Kormendy, J., & Kennicutt, R. C., Jr. 2004, ARA&A, 42, 603
Kosec, P., Pasham, D., Kara, E., & Tombesi, F. 2023, ApJ, 954, 170
Laha, S., Meyer, E., Roychowdhury, A., et al. 2022, ApJ, 931, 5
Laurenti, M., Luminari, A., Tombesi, F., et al. 2021, A&A, 645, A118
Lei, W.-H., Zhang, B., & Gao, H. 2013, ApJ, 762, 98
Leloudas, G., Dai, L., Arcavi, I., et al. 2019, ApJ, 887, 218
Levan, A. J., Tanvir, N. R., Brown, G. C., et al. 2016, ApJ, 819, 51
Levan, A. J., Tanvir, N. R., Cenko, S. B., et al. 2011, Sci, 333, 199
Li, R., Ho, L. C., Ricci, C., et al. 2022, ApJ, 933, 70
Liu, F. K., Li, S., & Chen, X. 2009, ApJL, 706, L133
Liu, F. K., Li, S., & Komossa, S. 2014, ApJ, 786, 103
Lodato, G., King, A. R., & Pringle, J. E. 2009, MNRAS, 392, 332
Loeb, A., & Ulmer, A. 1997, ApJ, 489, 573
Lu, W., & Bonnerot, C. 2020, MNRAS, 492, 686
Makishima, K., Maejima, Y., Mitsuda, K., et al. 1986, ApJ, 308, 635
Mangano, V., Burrows, D. N., Sbarufatti, B., & Cannizzo, J. K. 2016, ApJ, 817, 103
Martin, D. C., Fanson, J., Schiminovich, D., et al. 2005, ApJL, 619, L1
Masci, F. J., Laher, R. R., Rusholme, B., et al. 2019, PASP, 131, 018003
Masterson, M., Kara, E., Ricci, C., et al. 2022, ApJ, 934, 35
McKinney, J. C., Tchekhovskoy, A., & Blandford, R. D. 2012, MNRAS, 423, 3083
Metzger, B. D. 2022, ApJL, 937, L12
Metzger, B. D., & Stone, N. C. 2016, MNRAS, 461, 948
Miller, J. M., Kaastra, J. S., Miller, M. C., et al. 2015, Natur, 526, 542
Miller, J. S., & Stone, R. P. S. 1993, The Kast Double Spectrograph 66, Lick Observatory
Miller, M. C. 2015, ApJ, 805, 83
Mummery, A. 2021, MNRAS, 507, L24
Mummery, A., van Velzen, S., Nathan, E., et al. 2024, MNRAS, 527, 2452
Narayan, R., Igumenshchev, I. V., & Abramowicz, M. A. 2003, PASJ, 55, L69
Nardini, E., Reeves, J. N., Gofford, J., et al. 2015, Sci, 347, 860
NASA High Energy Astrophysics Science Archive Research Center (Heasarc), 2014 HEAsoft: Unified Release of FTOOLS and XANADU, Astrophysics Source Code Library, ascl:1408.004
Nixon, C., King, A., Price, D., & Frank, J. 2012, ApJL, 757, L24
Nordin, J., Brinnel, V., van Santen, J., et al. 2019, A&A, 631, A147
Okajima, T., Soong, Y., Balsamo, E. R., et al. 2016, Proc. SPIE, 9905, 99054X
Oke, J. B., Cohen, J. G., Carr, M., et al. 1995, PASP, 107, 375
Oke, J. B., & Gunn, J. E. 1982, PASP, 94, 586
Ouellette, N. N.-Q., Courteau, S., Holtzman, J. A., et al. 2022, MNRAS, 514, 2356
Pasham, D. R., Lucchini, M., Laskar, T., et al. 2023, NatAs, 7, 88
Pasham, D. R., Tombesi, F., Suková, P., et al. 2024a, SciA, 10, eadj8898
Pasham, D. R., Zajaček, M., Nixon, C. J., et al. 2024b, Natur, 630, 325
Perley, D. A. 2019, PASP, 131, 084503
Perley, D. A., Fremling, C., Sollerman, J., et al. 2020, ApJ, 904, 35
Phinney, E. S. 1989, in IAU Symp. 136, The Center of the Galaxy, ed. M. Morris (Cambridge: Cambridge Univ. Press), 543
Prugniel, P., & Soubiran, C. 2001, A&A, 369, 1048
Prugniel, P., Soubiran, C., Koleva, M., & Le Borgne, D. 2007, arXiv:astro-ph/0703658
Raftery, A. E. 1995, Sociol. Methodol., 25, 111
Raj, A., & Nixon, C. J. 2021, ApJ, 909, 82
Raj, A., Nixon, C. J., & Doğan, S. 2021, ApJ, 909, 81
Rees, M. J. 1988, Natur, 333, 523
Remillard, R. A., Loewenstein, M., Steiner, J. F., et al. 2022, AJ, 163, 130
Rest, S., Rest, A., Kilpatrick, C. D., et al. 2024, arXiv:2405.03747
Reynolds, C. S., Kara, E. A., Mushotzky, R. F., et al. 2023, Proc. SPIE, 12678, 126781E
Ricarte, A., Natarajan, P., Dai, L., & Coppi, P. 2016, MNRAS, 458, 1712
Ricci, C., Kara, E., Loewenstein, M., et al. 2020, ApJL, 898, L1
Ricci, C., Loewenstein, M., Kara, E., et al. 2021, ApJS, 255, 7
Ricci, C., & Trakhtenbrot, B. 2023, NatAs, 7, 1282
Rigault, M., Neill, J. D., Blagorodnova, N., et al. 2019, A&A, 627, A115
Roming, P. W. A., Kennedy, T. E., Mason, K. O., et al. 2005, SSRv, 120, 95
Roth, N., & Kasen, D. 2018, ApJ, 855, 54
Roth, N., Kasen, D., Guillochon, J., & Ramirez-Ruiz, E. 2016, ApJ, 827, 3
Saxton, C. J., Soria, R., Wu, K., & Kuin, N. P. M. 2012, MNRAS, 422, 1625
Saxton, R., Komossa, S., Auchettl, K., & Jonker, P. G. 2020, SSRv, 216, 85
Saxton, R. D., Read, A. M., Esquej, P., et al. 2012, A&A, 541, A106
Saxton, R. D., Read, A. M., Komossa, S., et al. 2017, A&A, 598, A29
Sądowski, A., & Narayan, R. 2016, MNRAS, 456, 3929
Schlafly, E. F., & Finkbeiner, D. P. 2011, ApJ, 737, 103
Schwarzenberg-Czerny, A. 1996, ApJL, 460, L107
Sheinis, A. I., Bolte, M., Epps, H. W., et al. 2002, PASP, 114, 851
Shen, R.-F., & Matzner, C. D. 2014, ApJ, 784, 87
Shingles, L., Smith, K. W., Young, D. R., et al. 2021, TNSAN, 7, 1
Shiokawa, H., Krolik, J. H., Cheng, R. M., Piran, T., & Noble, S. C. 2015, ApJ, 804, 85
Shu, X., Zhang, W., Li, S., et al. 2020, NatCo, 11, 5876
Silverman, J. M., Foley, R. J., Filippenko, A. V., et al. 2012, MNRAS, 425, 1789
Skrutskie, M. F., Cutri, R. M., Stiening, R., et al. 2006, AJ, 131, 1163
Smith, K. W., Smartt, S. J., Young, D. R., et al. 2020, PASP, 132, 085002
Somalwar, J. J., Ravi, V., Yao, Y., et al. 2023, arXiv:2310.03782
Steinberg, E., & Stone, N. C. 2024, Natur, 625, 463
Steiner, J. F., Narayan, R., McClintock, J. E., & Ebisawa, K. 2009, PASP, 121, 1279
Stone, N., & Loeb, A. 2012, PhRvL, 108, 061302
Strubbe, L. E., & Quataert, E. 2009, MNRAS, 400, 2070
Strüder, L., Briel, U., Dennerl, K., et al. 2001, A&A, 365, L18
Takeuchi, S., Ohsuga, K., & Mineshige, S. 2013, PASJ, 65, 88
Tchekhovskoy, A., & McKinney, J. C. 2012, MNRAS, 423, L55
Tchekhovskoy, A., Metzger, B. D., Giannios, D., & Kelley, L. Z. 2014, MNRAS, 437, 2744
Tchekhovskoy, A., Narayan, R., & McKinney, J. C. 2011, MNRAS, 418, L79
Teboul, O., & Metzger, B. D. 2023, ApJL, 957, L9
Thomsen, L. L., Dai, L., Kara, E., & Reynolds, C. 2022a, ApJ, 925, 151
Thomsen, L. L., Kwan, T. M., Dai, L., et al. 2022b, ApJL, 937, L28
Tombesi, F., Cappi, M., Reeves, J. N., et al. 2010, A&A, 521, A57
Tombesi, F., Meléndez, M., Veilleux, S., et al. 2015, Natur, 519, 436
Tombesi, F., Sambruna, R. M., Marscher, A. P., et al. 2012, MNRAS, 424, 754
Tonry, J., Denneau, L., Weiland, H., et al. 2022, TNSTR, 2022-1521, 1
Tonry, J. L., Denneau, L., Heinze, A. N., et al. 2018, PASP, 130, 064505
Trakhtenbrot, B., Arcavi, I., MacLeod, C. L., et al. 2019, ApJ, 883, 94
Trumper, J. 1982, AdSpR, 2, 241
Ulmer, A. 1999, ApJ, 514, 180
van der Walt, S., Crellin-Quick, A., & Bloom, J. 2019, JOSS, 4, 1247
van Velzen, S., Gezari, S., Cenko, S. B., et al. 2019, ApJ, 872, 198
van Velzen, S., Gezari, S., Hammerstein, E., et al. 2021, ApJ, 908, 4
van Velzen, S., Holoien, T. W. S., Onori, F., Hung, T., & Arcavi, I. 2020, SSRv, 216, 124
VanderPlas, J. T. 2018, ApJS, 236, 16
Vigneron, Q., Lodato, G., & Guidarelli, A. 2018, MNRAS, 476, 5312
Virtanen, P., Gommers, R., Oliphant, T. E., et al. 2020, NatMe, 17, 261
Voges, W., Aschenbach, B., Boller, T., et al. 1999, A&A, 349, 389
Wang, Y., Baldi, R. D., del Palacio, S., et al. 2023, MNRAS, 520, 2417
Wevers, T., Guolo, M., Pasham, D. R., et al. 2024, ApJ, 963, 75
Wilms, J., Allen, A., & McCray, R. 2000, ApJ, 542, 914
Wright, E. L., Eisenhardt, P. R. M., Mainzer, A. K., et al. 2010, AJ, 140, 1868
Yao, Y. 2022, TNSCR, 45, 1
Yao, Y., De, K., Kasliwal, M. M., et al. 2020, ApJ, 900, 46
Yao, Y., Lu, W., Guolo, M., et al. 2022a, ApJ, 937, 8
Yao, Y., Lu, W., Harrison, F., et al. 2024, ApJ, 965, 39
Yao, Y., Miller, A. A., Kulkarni, S. R., et al. 2019, ApJ, 886, 152
Yao, Y., Ravi, V., Gezari, S., et al. 2023, ApJL, 955, L6
Yao, Y., Somalwar, J., Stein, R., et al. 2022b, TNSAN, 223, 1